

TOPICAL REVIEW

Atomic nanofabrication: atomic deposition and lithography by laser and magnetic forces

D Meschede and H Metcalf¹Institut für Angewandte Physik, Rheinische Friedrich-Wilhelms-Universität Bonn,
Wegelerstr. 8, D-53115 Bonn, Germany

Received 8 October 2002

Published 15 January 2003

Online at stacks.iop.org/JPhysD/36/R17**Abstract**

Atomic deposition on a surface can be controlled at the nanometre scale by means of optical and magnetic forces. Impingement of atoms on the surface can lead to growth of a structured array (direct deposition) or to chemical modifications of the surface (neutral atom lithography). In this report we survey requirements, present the current results, and explore the potential applications of this method of nanofabrication.

1. Introduction*1.1. Background*

The advent of laser cooling in the 1980s has stimulated the development of many different methods to control the motion of free, neutral atoms using forces that arise from their interaction with laser light or magnetic fields [1]. Laser cooling has provided atomic beams with low velocities (kinetic energies), and has strongly enhanced their brightness, brilliance and phase space density [2]. As a result, even feeble forces such as the dipole force of laser light acting on an induced atomic dipole moment, and magnetic forces on paramagnetic atoms, can now be used for precise control of the motion of atoms in beams. This has given rise to the field of atom optics.

The original developments of atom optics date back to the early days of atomic beams in the 1920s when inhomogeneous magnetic fields acted on atomic magnetic moments in the famous experiments by Stern and Gerlach [3, 4]. Only a few years later Frisch performed a similarly pioneering experiment in atom optics by deflecting an atomic beam with light pressure [5]. However, the development of truly useful atom optical elements such as lenses and mirrors only became possible after laser cooling had provided the methods for precise control of atomic motion [6].

Atom optical tools are now being explored for various applications. One of these is the production of patterns and

of images generated by atomic beams incident on suitable surfaces. Generating structures this way should appropriately be called atomic nanofabrication (ANF). Such arrays have intrinsic nanometre dimensions since the typical scale of optical interferences is of the order of half wavelength, i.e. in the sub-micrometre domain. Hence, it is interesting to explore the potentials and physical limits of nanostructure manufacturing with current and foreseeable atomic beam technology.

Successful ANF requires suitably prepared atomic samples that can be manipulated in the desired way, and the techniques for such manipulation. The most common method is to exploit the capabilities of lasers for both sample preparation and atom manipulation. Needless to say, the requirements of the light beams for such disparate purposes are usually sufficiently different that a single laser cannot be used for both. In fact, it is more often the case that multiple laser beams are needed for each purpose.

Magnetic forces offer an alternative route towards control of atomic motion, albeit not intrinsically at nanometre scales. Magnetic atom optical elements have been constructed many decades ago [7–9]. Imaging applications, however, have only become possible since atomic beams with well controlled properties became available through laser cooling [10]. An interesting question is whether magnetic lenses and mirrors can be constructed to such a precision that sub-micron imaging applications become feasible. Magnetic guides at the micron scale have already been demonstrated indicating prospects of this force [11].

¹ Permanent address: Physics Department, Suny, Stony Brook, NY 11794-3800, USA.

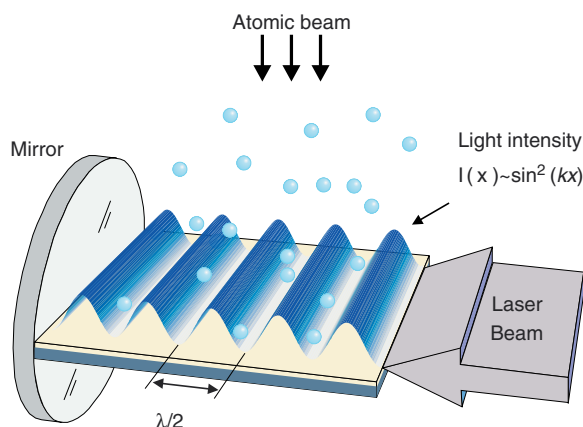


Figure 1. Basic concept of ANF.

The purpose of this paper is to review the present status of the different branches of the experimental art of ANF, and to discuss further possible applications. Basic properties of ANF can be well understood with a simple one-dimensional standing wave which is thus extensively treated, as is also the case in experiments. Two-dimensional and even three-dimensional nanofabrication aspects make an attractive application of ANF and are discussed as well.

1.2. Early ANF experiments

The simplest example of ANF by optical forces is obtained using a standing wave light field serving as an immaterial focusing mask on a suitable substrate, as shown in figure 1. The energy levels of atoms are shifted as they pass through the light field. This light shift is zero at the nodes, but not elsewhere so its spatial non-uniformity corresponds to a spatially varying potential whose gradient results in a force. For the case shown in figure 1, this force is along the direction of the \mathbf{k} -vectors of the standing wave. Because of these optical forces on the incident atoms, the standing wave acts as an array of microscopic lenses with apertures of the order of the wavelength of light. These lenses focus appropriately directed atoms in an incident beam toward the optical nodes or antinodes, depending on the sign of the difference between the atomic and laser frequencies.

This method was first implemented by Timp and colleagues with a beam of sodium atoms deposited on a glass substrate [12]. Because of the chemical instability of sodium in air, their fabricated structure could not survive removal from the vacuum chamber. A significant advance was later achieved when McClelland and co-workers [13] successfully applied the method to chromium atoms, and showed that both high resolution (below 100 nm) and external processing of extended surfaces were possible.

In both of these experiments, atoms were deposited in an array of lines on a surface with a structure transferred from the gradient of the intensity distribution of the standing wave light field applied above the surface acting as an immaterial focusing or proximity mask (see figure 1). This direct deposition (DD) technique forms one of the two main branches of ANF. It has been extended to make atomic arrangements in two dimensions [14, 15], and appears to offer unique promises for

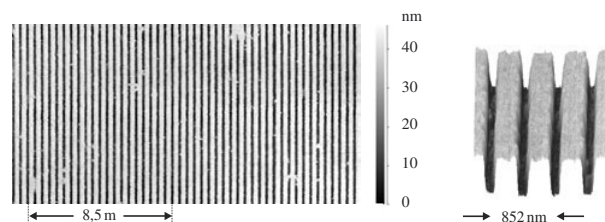


Figure 2. Arrays of straight lines of gold manufactured by cesium NAL. The image was obtained with an AFM (see text for details) [22].

the application of ANF to much more sophisticated structures [16–18].

While such DD techniques produce a physical surface modification, the second branch of ANF causes chemical modification of a surface. Berggren and co-workers [19] have demonstrated the modification of the chemical properties of a thin film made from a self-assembled monolayer (SAM) of organic molecules on a surface. They used a beam of metastable argon atoms patterned by a mechanical mask instead of by optical forces as described above. After wet etching, the structure of the shadow mask was precisely reconstructed.

This method of neutral atom lithography (NAL) is completely analogous to ordinary resist-based methods such as optical or e-beam technologies that are at the heart of most conventional lithography processes [20]. Such NAL has been implemented with other atoms [21], and it was also successfully combined with the use of immaterial (i.e. optical) light masks [22] (see figure 2) and the exploitation of degrees of freedom associated with internal atomic structure [23].

There are important similarities and differences between the two branches of ANF, DD and NAL. Obviously, in both cases atomic samples are required that can conveniently be formed into beams and that have optical transitions that are readily accessible with available lasers. Differences are determined by the interaction with the surface. In DD atom arrivals must be accumulated for growth of structures, while in NAL atoms cause local chemical modification of the surface. As a consequence, NAL can be applied to a much wider range of substances, including organic materials. The only requirements are vacuum compatibility and etching ability. Another important similarity of both branches is that the structure formation is strongly affected by migration, agglomeration and local interaction of the atoms deposited on the surface. Although the explicit behaviour of such properties has not been widely investigated, details of the atom–surface interaction will certainly play a crucial role in the future applications of ANF. Note that DD growth is quite different from typical epitaxial growth, where the aim is to deposit smoothly several uniform layers having no transverse structure [24].

2. Light masks for ANF

2.1. Optical dipole forces

Dissipative light forces are necessary for the laser cooling that prepares atomic beams with a small solid angle of divergence

(or beam spread) $\Delta\Omega$, and enhanced flux density \mathcal{F}/A (see section 3.1). By contrast, conservative dipole forces that derive from the gradient of the light shift are primarily used for steering atoms into the desired patterns for ANF [6]. These gradients typically arise in a light field constructed from several beams propagating in different directions. The use of a such a spatially modulated light field as an immaterial, defect-free mask to transform its intensity distribution to a pattern on a substrate has contributed to the interest aroused by this method of nanofabrication.

The optical dipole force acting on an atom with resonance frequency ω_A in a laser field of detuning $\delta = \omega_L - \omega_A$ is derived from the spatial variation of the light shift $\omega_{ls}(\mathbf{r})$ [1]. For a single laser beam travelling in the x -direction with Rabi frequency Ω , the light shift is given by

$$\omega_{ls} = \frac{\sqrt{\Omega^2 + \delta^2} - \delta}{2}. \quad (1)$$

For sufficiently large detuning $\delta \gg \Omega$, approximation of equation (1) leads to $\omega_{ls} \approx \Omega^2/4\delta = \gamma^2 s/8\delta$, where $s \equiv I/I_{\text{sat}}$, I is the laser beam intensity, $I_{\text{sat}} \equiv \pi\hbar c/3\lambda^3\tau$ is the saturation intensity, and $\tau \equiv 1/\gamma$ is the atomic excited state lifetime.

In a standing wave with $\delta \gg \Omega$, $\omega_{ls} = \omega_{ls}(x)$ varies sinusoidally from node to antinode and also spontaneous emission is inhibited so that $\hbar\omega_{ls}(x)$ may be treated as a potential $U(x)$. The resulting dipole force is

$$\mathbf{F}(x) = -\nabla U(x) = -\frac{\hbar\gamma^2}{8\delta I_{\text{sat}}}\nabla I(x) \equiv U_{\text{max}}\nabla f(x), \quad (2)$$

where $I(x) = I_{\text{max}}f(x)$ is the total intensity distribution of the standing wave light field of period $\lambda/2$, I_{max} is the maximum intensity, and $f(x)$ describes the normalized modulation of the light field. For such a standing wave, the optical electric field (and the Rabi frequency) at the antinodes is double that of each travelling wave that composes it, and so the total intensity I_{max} at the antinodes is four times that of the single travelling wave.

Once the light field intensity distribution is known, atomic trajectories may be calculated from purely classical equations of motion. From these calculations, atom optical properties can be numerically studied with sufficient precision to understand their basic properties. Figure 3 shows an example of an atomic beam focused using the dipole forces of a standing wave beam.

2.2. Properties of a single standing wave atom lens

The simplest possible light force lens is formed by a one-dimensional standing wave, as shown in figure 1. The dipole potential of equation (2) is given by $U(x) = U_{\text{max}}\sin^2 kx$, and a single lens extends from $x = -\lambda/4$ to $x = +\lambda/4$. In the vicinity of $x = 0$, we find harmonic oscillations with a period $T_{\text{osc}} = 2\pi\sqrt{M/U''}$ where $U'' \equiv \partial^2 U(x)/\partial x^2|_{x=0}$ and M = atomic mass. A Gaussian intensity profile given by $I(z) = I_{\text{max}}\exp(-z^2/w_0^2)$, w_0 is the beam waist radius, is assumed in the z -direction, but may be replaced by a square profile for some simple estimates.

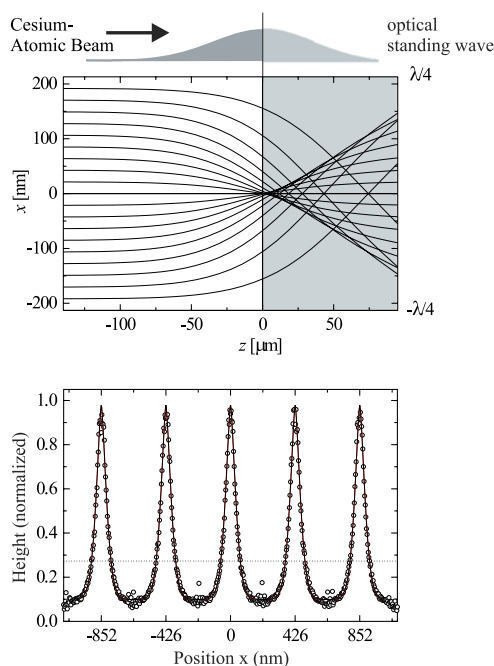


Figure 3. Top: Numerically calculated trajectories of a laser-cooled beam of atoms focused to the centre of a Gaussian envelope standing wave light field (thick lens limit). The focused laser beam forming the optical standing wave is clipped by the substrate. Note the different scales in x - and z -directions. Bottom: Analysis [25] of flux concentration for a realistic beam of thermal cesium atoms with 0.1 m s^{-1} transversal rms velocity at the focal plane $z = 0$. The dotted line shows the flux distribution without the standing optical wave.

2.2.1. Thin lenses, thick lenses. There are two quite different limiting cases for the focusing of atoms moving through such a standing wave light field, in close correspondence with conventional optics. In the ‘thin lens’ limit, the atomic displacement while in the light field is small compared to the initial value of x , and after leaving the light field, atoms travel a considerable distance to the substrate. In this case, their transverse velocity is changed by $\Delta v_{\perp}(x) = 2F(x)w_0/Mv_{\ell}$ (where the longitudinal velocity $v_{\ell} \gg \Delta v_{\perp}$) and so atoms moving initially parallel to the x -axis cross it at a distance [26]

$$z = f_{\text{thin}} = x \frac{v_{\ell}}{\Delta v_{\perp}} = \frac{\text{KE}}{2w_0 U''}, \quad (3)$$

where KE is their kinetic energy.

In the opposite limit (‘thick lens’) the light force atom lens closely resembles the graded index (GRIN) lens of traditional optics. The atoms cross the x -axis while still in the light field and thus still subject to the optical dipole force. Replacing the Gaussian beam profile with a constant intensity value, we find that the atoms cross the x -axis at a distance

$$z = f_{\text{thick}} = \frac{v_{\ell} T_{\text{osc}}}{4} = \pi \sqrt{\frac{\text{KE}}{2U''}}. \quad (4)$$

While f_{thin} and f_{thick} are very different kinds of quantities, in both cases they are calculated for the paraxial approximation. For strong focusing, we need a short focal length f and hence the thick lens regime is desirable. Inspection of

equations (3) and (4) furthermore shows that the dependence on chromatic aberrations (\sqrt{q} vs q where $q = KE/U''$) is reduced in this case, too.

Increasing the dipole force (e.g. by reducing the detuning $|\delta|$ or increasing the intensity $I(x)$) will take the light force lens from the thin to the thick limit, and at still higher intensities into the ‘channelling’ regime where atoms experience multiple oscillations while traversing the lens. Numerical analysis shows, however, that in the thick lens limit and contrary to expectations, increasing power no longer decreases the focal length in the usual Gaussian beam profile since focusing already occurs during the entry into the wings of the light field (for details see [26]) and the principal planes simply move out of the centre.

Focusing to the centre of the light field is a desirable experimental configuration. The laser power P_{ANF} required to realize such focusing does not depend on the radius w_0 of the Gaussian beam ([26], equation (23), where $\omega_r = \hbar k^2/2M$ is the recoil frequency).

$$P_{\text{ANF}} = 5.37 \frac{\pi I_{\text{sat}} \delta v_\ell^2}{4\omega_r \gamma^2} \quad (5)$$

and hence allows for variation of the focal length. In table 2 in section 3.1, we have collected characteristic values for P_{ANF} at detuning $\delta 2\pi = 200$ MHz, showing moderate power requirement.

In figure 3, the light force lenses concentrates the atomic flux exactly at the centre of the Gaussian beam profile by a suitable choice of parameters according to equation (5). Both good contrast and sharp focusing are achieved for the paraxial rays of the perfectly collimated atomic beam. To be specific about the deposition result we have defined in figure 4 characteristic parameters primarily for the DD branch of ANF. (For NAL the quantities can be used in close analogy.) The feature ‘width’ Δx may expressed in terms of the period, or natural scale length $\lambda/2$,

$$\Delta x = \alpha \frac{\lambda}{2}. \quad (6)$$

For most nanofabrication processes it is desirable to make the feature width as small as possible, e.g. $\alpha < 1/10$. Other applications such as the bottom-up growth of photonic crystals which requires an index of refraction modulation at the wavelength scale might tolerate much wider features provided good contrast is achieved.

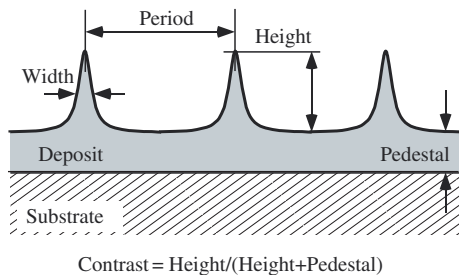


Figure 4. Characterization of deposited atomic material, mainly for DD.

2.2.2. Imaging distortions. In reality, the width of the features is broadened and the contrast is reduced as a consequence of several physical phenomena:

- The atomic beam is not perfectly collimated and hence trajectories with different initial inclinations are focused away from the axis.
- For $|x| > \lambda/8$ the harmonic approximation begins to fail, and as shown in figure 3, atoms are not well focused as a result of ‘spherical aberration’.
- Atoms travel at different velocities leading to different focal lengths (see, equations (3) and (4)).
- In the wave regime the Rayleigh diffraction limit of focusing may play a role.

The feature width depends crucially on focusing distortions as listed in table 1 and discussed below. The fidelity of the imaging process in standing waves has been described in great detail in [27, 26, 28] and will only be summarized here.

Beam divergence. The consequence of collimation of the atomic beam with angular spread 2θ can be anticipated from geometrical optics for a thin lens that predicts the smear of the image size to be $\Delta x \approx f\theta$, where f is the focal length of the image-forming lens and x is along the \mathbf{k} -vectors of the standing wave light beams.

In the usual experimental configuration, f is chosen to equal the focusing laser beam’s waist size w_0 , typically 100λ . In [26, 28], it is shown that even in this ‘thick lens’ limit, the focal position of atoms approaching the lens array at an angle θ will be displaced from those with $\theta = 0$ by $x = f\theta$, just as in the thin lens case. Then the focal spot will be smeared by $w_0\theta$. Thus for an array of lenses as shown in figure 1, in the usual experimental configuration with $f = w_0$, production of features of size $\alpha\lambda/2$ requires $\theta < \alpha\lambda/4w_0$. This is a rather stringent requirement because the desired value of α may very well be $\alpha \sim 1/10$, and the consequent $\theta < 0.3$ mrad is about at or below the limit for Doppler cooling of a beam having $\bar{v}_\ell \sim 400$ m s⁻¹. These estimates are supported by numerical calculations both in [26, 28] and our own simulations.

The preparation of a well-collimated and transversely cooled beam is hence essential to minimize the severely deleterious effects of even a small angular spread. Effects of atomic beam divergence generally dominate the limits to the minimum feature size.

Table 1. Summary of distortions of focusing by a standing wave dipole force lens. Except for ‘spherical aberration’, which produces a pedestal and thereby reduces contrast, all other phenomena tend to increase the feature size.

Imaging distortion	Short comments
Spherical aberration	Generates and dominates pedestal
Chromatic aberration	Dominant but tolerable even for thermal beams
Beam spread θ	Broadening to $f \cdot \theta$, control by laser cooling
Surface diffusion	Depends on material and temperature
Spontaneous emission	Contributes to beam spread, control by detuning
Diffraction	Negligible for thermal beams, essential for matter waves

Spherical aberrations. Spherical aberrations of the thin lens case have been analysed in [27, 29] and a numerical extension to the thick lens regime is given in [26, 29]. The latter does not result in an analytic formula but leads by inspection of the results to the conclusion that the spherical aberration contributes by rendering a small unfocused pedestal but does not significantly broaden the focused part. Attempts have been made [30] to experimentally control spherical aberration by supplementing the light field with a mechanical field mask aligned with the light mask. According to the conclusion drawn here this measure should result in an improved contrast, not a narrower feature.

Chromatic aberrations. In the thin lens regime, the Maxwellian velocity distribution of atoms from a thermal source leads to strong chromatic aberration of atom optical components. Numerical analysis shows the surprising result in the thick lens regime, however, that even for a thermal beam with $\bar{v}/\Delta v_\ell \approx 1$ the chromatic distortion on feature size is still tolerable, that in fact beam spread is dominant unless controlled by transverse laser cooling. The numerical analysis is supported by the experimental observation [28] that with increasing light intensity of the lens, the feature width falls to a minimum but only slowly grows again.

The moderate role of spherical and chromatic aberrations in comparison with beam spread is surprising. As a consequence of these considerations, atomic beams with narrowed velocity spread, although available experimentally, e.g. by supersonic expansion or by longitudinal laser cooling [2] do not offer significant advantages in the focusing properties of light masks.

Diffraction limit. At 200 ms^{-1} , the atomic de Broglie wavelengths are typically $< 50 \text{ pm}$, and so the numerical aperture of the focusing lenses in the array given by $\lambda/4w_0 \sim 1/400$ gives a de Broglie wave diffraction limit of $< \lambda/40$, not far from the value $\alpha = 1/10$ discussed above. As with the estimate for θ , this estimate for Δx is also supported by numerical calculations, both in [26] and our own simulations. A detailed quantum mechanical analysis is given in [31].

Spontaneous emission and heating. Atoms experience transverse heating caused by recoil from spontaneous emission. Heating contributes to the beam spread, but can always be kept small by choosing sufficiently large detuning.

Surface physics and chemistry. In addition to the distortions caused by deviations of atomic trajectories from their idealized path, the physical and chemical interaction of the atoms with the surface will further modify the structural properties generated. In contrast to well-known molecular beam epitaxy (MBE) where the experimental aim is to obtain atomically flat and homogeneous surfaces, ANF attempts to generate structured and inhomogeneous surfaces in a well controlled way. Formation of terraces is obviously influenced by the dynamics of surface adsorbed atoms and was studied for instance by [32, 33]. Very recently there have been attempts [24, 34, 35] to understand the formation of ANF features including atomic dynamics (agglomeration, diffusion) which may cause either enhanced or reduced broadening of focal lines in DD.

In NAL, after the exposure step there are always conventional chemical processes necessary in order to recover the structure imposed, and details of the chemical interaction will determine the structural parameters including feature width. Few investigations of these chemical interactions have been carried out to date (see, e.g. [36]).

2.2.3. Conclusion. Thus, we see how elementary considerations of the preparation of the atomic beam for ANF lead to an easily achievable set of parameters for the geometry and laser beam characteristics for ANF in one dimension with typical atoms. Appropriate consideration must be given for different atoms and geometries, and so the sources of these estimates are provided above. Considerable data for many atoms is readily available [1].

3. Atomic beams for ANF

The application of atom optics for DD or NAL depends on the availability of suitable beams with sufficient control of atomic velocities, so this section will briefly review their current status. The important parameters for the suitability of a beam for ANF include the total atomic flux \mathcal{F} and the distribution of atomic velocities, both longitudinal (monochromaticity) and transverse (collimation).

3.1. Atomic flux and beam collimation

The amount of atomic flux needed for efficient ANF depends on the particular application because there are at least two competing factors. On the one hand, only a small part of the substrate surface needs to be exposed to reproduce the desired pattern. For example, writing lines of width Δx in a resist for NAL as in figure 2 requires an exposure of the fraction $2\Delta x/\lambda = \alpha < 1$ of the total surface. On the other hand, the required dosage per surface unit (surface atom, molecule, unit cell) may be larger than one atom. For NAL it's typically a few atoms, but for DD, a significant buildup surely requires very many atoms per surface unit. An estimate of the necessary flux might be guessed by choosing an average of at least one atom per surface unit. Providing this dosage across a square millimetre of surface with a site density of $6 \times 10^{12} \text{ mm}^{-2}$ (4 \AA unit cell) requires an incident flux density of $10^{11} \text{ atoms mm}^{-2} \text{ s}^{-1}$ to reduce exposure times to below 1 min, a rough measure of feasibility for reasonable applications.

Besides the total flux \mathcal{F} (atoms s^{-1}) and flux density \mathcal{F}/A , where A is the beam cross section, other important atomic beam properties are brilliance \mathcal{B} and brightness (or also radiance) \mathcal{R} , given by

$$\mathcal{B} = \frac{\mathcal{F}}{A} \frac{1}{\Delta\Omega} \frac{\bar{v}_\ell}{\Delta v_\ell} = \mathcal{R} \frac{\bar{v}_\ell}{\Delta v_\ell}. \quad (7)$$

Here, $\Delta\Omega$ is the solid angle of divergence, and $\bar{v}_\ell/\Delta v_\ell$ is the longitudinal velocity spread. Brilliance is related to the universal phase space density Λ (the number of atoms per unit phase space volume \hbar^3) through $\Lambda = \pi \mathcal{B}/M^3 \bar{v}_\ell^4$ (M is the atomic mass) [2].

Although these quantities may be the appropriate figures of merit for many experiments, especially in the quantum gas regime such as BEC studies, they are not the best choice

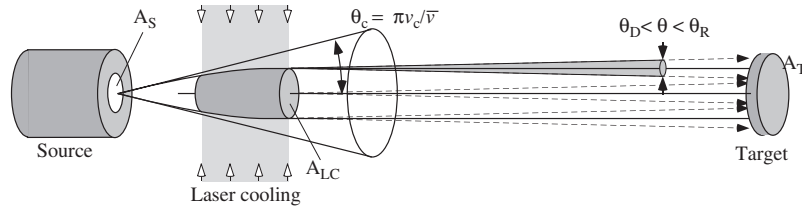


Figure 5. Parameters of an atomic beam for ANF.

to describe the suitability of atomic beams for ANF. This is because they can increase without limit as either $\Delta\Omega$ or Δv_ℓ approach zero. Although $\Delta\Omega$ or Δv_ℓ need to be small for good ANF, there are lower limits described in section 2.2.2 beyond which the quality of structures fabricated by ANF does not improve. In such a domain, \mathcal{B} or \mathcal{R} could increase without any benefit to ANF. Although ANF is frequently suggested as an interesting application of coherent matter waves with the ultimate brightness and phase space density, this subject remains completely unexplored to date. In chapter 6, we briefly discuss the prospects of atomic matter waves in ANF.

Besides connecting them to more fundamental quantities, the three factors of \mathcal{B} in equation (7) indicate the relevance of different atomic beam properties which we will now treat separately. An outline of essential properties determining parameters of the laser collimated atomic beams is shown in figure 5.

3.1.1. Flux density (\mathcal{F}/A). In traditional atomic beams, this factor is determined by geometry only, e.g. for paraxial beams the flux density of the source, \mathcal{F}_S/A_S , is reduced to the value \mathcal{F}_T at the target where $\mathcal{F}_T = 2\mathcal{F}_S(A_T/\pi R^2)$, the target area is A_T , and it's at distance² R . Transverse laser cooling, or optical collimation, however, can capture all atoms with transverse velocities below $v_c \sim \gamma/k = \lambda/2\pi\tau$, thus significantly enhancing the effective solid angle to $\Delta\Omega_{\text{cap}} = \pi(v_c/\bar{v}_\ell)^2$. In the absence of laser cooling, atoms effusing from the source that would irradiate a surface area $A_c = \Delta\Omega_{\text{cap}}R^2$ are now concentrated onto the target.

The flux density for a laser-cooled beam (LC) can be estimated from $\mathcal{F}_T^{\text{LC}} = (A_c/A_T)\mathcal{F}_T = 2\mathcal{F}_S(v_c/\bar{v}_\ell)^2$ resulting in a substantial laser cooling enhancement factor $G_{\text{LC}} = (v_c/\bar{v}_\ell)^2(\pi R^2/A_T)$. Typical values are $v_c/\bar{v}_\ell \sim 10^{-2}$, $A_T \approx 1 \text{ mm}^2$, and $R \sim 0.5 \text{ m}$ so $G_{\text{LC}} \sim 80$. Figure 6 shows the flux density enhancement by a factor of 25 for a cesium atomic beam. Large capture velocities are obtained through Doppler cooling while ultimately small transverse velocities are obtained by sub-Doppler processes (see section 3.1.2). Although the lowest temperature achievable by Doppler cooling occurs for a laser detuning $\delta \equiv \omega_L - \omega_A = -\gamma/2$ (red of atomic resonance), the magnitude of v_c increases with $|\delta|$. Since the efficacy of laser cooling decreases with increasing $|\delta|$, a reasonable compromise is $\delta = -2\gamma$, and then a suitable choice is $s = 2$.

The capture and collimation process will permit even a point-like source to expand into a beam with diameter $2r_c \sim v_c\tau_c$ and cross section $A_{\text{LC}} = \pi r_c^2$ where the diameter $2r_c$ is of order 1 mm or below for all elements. Since large flux density

² One might expect a factor $A_T/4\pi R^2$ here. A factor 4 is caused by the cos-distribution emanating from the source and favouring the forward direction.

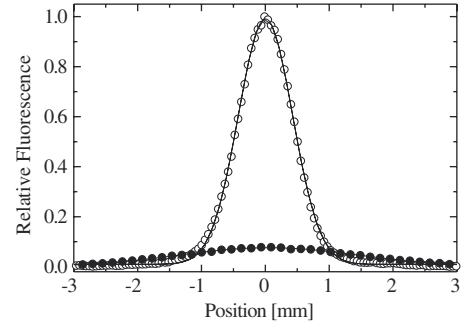


Figure 6. Cross section of cesium atomic beam showing flux density enhancement (collimation) caused by two-dimensional transverse laser cooling with linear polarization at 45° (lin \perp lin-configuration) to the atomic beam and the direction of propagation for polarization gradient cooling. (\circ/\bullet): With/without cooling laser [25]. Solid lines are fits to Gaussian functions. Laser power 22 mW ($250 \mu\text{W}$ for repumping), full $1/e^2$ widths of laser beam $30 \times 8 \text{ mm}^2$; detection downstream 1.2 m from the cooling zone.

is desirable for ANF, the diameter of the source aperture should thus be chosen as large as the target area to be irradiated.

The velocity damping coefficient, defined by $F = -\beta v$ for Doppler molasses in a two-level atom, is given by [1]

$$\beta = -\frac{M\omega_r \cdot 16s(\delta/\gamma)}{[1 + (2\delta/\gamma)^2]^2}, \quad (8)$$

where $\omega_r \equiv \hbar k^2/2M$ is the atomic recoil frequency. The velocity damping time M/β for the parameters above is then $\sim 5/\omega_r$. The capture angle θ_c associated with such a choice is $(2\gamma/k)/\bar{v}_\ell$, typically 10–20 mrad. Thus it would also be of little value to place the cooling region much closer to the oven than a r_c/θ_c or several cm.

It is worth noting here that by tilting the collimation laser beams slightly from the perfect orthogonal to the beam axis, and using a combination of mechanical apertures, excellent separation of undesirable components from the laser collimated atomic beam may be achieved. Characteristic values for elements relevant to ANF are collected in table 2.

3.1.2. Collimation ($1/\Delta\Omega$). At the end of the laser collimation stage, the divergence of the atomic beam is determined by \bar{v}_ℓ and the transverse velocity distribution, or temperature resulting from laser cooling. The two limiting cases of Doppler (T_D) and recoil temperature (T_R) give rise to divergence angles $\theta_{D,R}$, respectively:

$$\theta_{D,R} = \sqrt{\frac{T_{D,R}}{T_S}} = \frac{v_{D,R}}{\bar{v}_\ell}. \quad (9)$$

Table 2. Parameters of atomic beams for ANF.

Atom	T_S (K)	λ (nm)	γ (10^7 s $^{-1}$)	v_c (m s $^{-1}$)	θ_c (mrad)	$5/\omega_r$ (μ s)	$2r_c$ (mm)	P_c (mW)	Θ_D (mrad)	Θ_R (mrad)	P_{ANF} (mW)
$^4\text{He}^*$	300	1083	1.0	1.7	1.5	19	0.03	0.03	0.36	0.11	0.40
^{23}Na	630	589	6.2	5.8	13	32	0.18	1.0	0.89	0.09	0.12
^{27}Al	1640	309	8.2	4.0	4.0	10	0.04	6	0.44	0.07	0.95
$^{40}\text{Ar}^*$	300	812	3.6	4.8	17	105	0.49	0.5	0.68	0.05	0.15
^{52}Cr	1825	426	3.1	2.1	3.5	37	0.08	2.4	0.26	0.03	2.0
^{56}Fe	1920	372	1.6	1.0	1.3	31	0.03	1.5	0.18	0.04	4.6
^{70}Ga	1555	403	4.9	3.1	5.2	45	0.14	4.3	0.35	0.03	1.1
		417	9.2	6.1	10	48	0.29	7.8	0.48	0.03	0.59
^{108}Ag	1435	328	1.4	7.2	15	46	0.33	18	0.61	0.03	0.46
^{115}In	1355	410	5.8	3.8	8.5	77	0.29	6.0	0.40	0.03	0.83
		451	10.2	7.3	16	93	0.68	9.5	0.54	0.02	0.43
^{133}Cs	410	852	3.3	4.5	20	383	1.7	3.3	0.55	0.02	0.21
^{197}Au	1800	268	16.7	7.1	19	57	0.40	32	0.59	0.04	0.60

Definitions: T_S : source temperature for a pressure of 0.1 Torr; $\bar{v}_\ell = \sqrt{2kT/M}$: average thermal velocity; $\lambda = 2\pi/k$: resonance wavelength; γ : spontaneous decay rate; $v_c = \gamma\lambda/2\pi$: capture velocity; $\theta_c = v_c/\bar{v}_\ell$: capture angle; $\omega_r = \hbar k^2/2M$: recoil frequency; $2r_c = 5v_c/\omega_r$: capture radius; $P_c = 1 \text{ mm} * (5\bar{v}_\ell/\omega_r) \cdot I_{\text{sat}}$, P_{ANF} evaluated with equation (5) and $\delta/2\pi = 200$ MHz: laser power required for collimation and focusing, respectively, with $I/I_{\text{sat}} = 1$ over the area of a 1 mm diameter atomic beam for a single laser beam folded for multiple use. For optimal results $I/I_{\text{sat}} \simeq 3\text{--}5$ is desirable; $\theta_{D,R} = v_{D,R}/\bar{v}_\ell$: beam spread angles.

Sub-Doppler cooling mechanisms have been described in some detail in [37, 1], and all atoms listed in table 2 are amenable to these methods. As discussed in section 2.2, excellent collimation is a necessary condition for obtaining narrow feature widths in ANF. In many cases, the Doppler limit may already be sufficient, but even moderate improvement by sub-Doppler cooling forces will generally lower the beam spread to an acceptable quality. Thus, we have

$$\theta_D \geq \theta_{\text{LC}} \geq \theta_r \quad \text{and} \quad \frac{1}{\Delta\Omega_{\text{LC}}} = \frac{1}{\pi\theta_{\text{LC}}^2}. \quad (10)$$

3.1.3. Monochromaticity ($\bar{v}_\ell/\Delta v_\ell$). A thermal beam is non monochromatic and has $\bar{v}_\ell/\Delta v_\ell \simeq 1$. Improvements of the monochromaticity can be obtained in supersonic beams ($>10:1$) or by longitudinal laser cooling (factors 500 have been experimentally demonstrated [2]). Longitudinal cooling of a thermal beam is, however, a demanding technical effort at the expense of reduced flux density, while it does not significantly reduce the influence of chromatic aberrations. We are led to the conclusion that transversely cooled, thermal beams remain the source of choice for ANF. Atomic matter waves are inherently monochromatic but will be discussed in section 6.

3.2. Atomic beam sources for ANF

We may distinguish three different types of atomic beam sources for ANF: thermal atomic beams with transverse laser cooling, variants of slow beams from a magneto-optical trap (MOT, in particular the so-called 2D $^+$ -MOT), and the new breed of atom lasers emitting coherent matter waves.

Laser-cooled thermal beams. Most experiments on ANF have been carried out with laser-cooled thermal beams that have been discussed in detail above. It is instructive to rewrite equation (7), evaluated for the target \mathcal{B}_T , for the case of thermal velocity spread $\bar{v}_\ell/\Delta v_\ell = 1$. Let us assume that all quantities except the source flux have values as achieved at the end of the

laser cooling stage as long as the separation to the target is small compared with $r_c/\theta_{D,R}$ —in other words all atoms from the laser-cooled stage will reach the target, as indicated in figure 5.

Then, we have $\mathcal{B}_T \simeq \mathcal{B}_{\text{LC}}$, and with $\mathcal{F}_T^{\text{LC}} = 2\mathcal{F}_S(v_c/\bar{v}_\ell)^2$, $A_{\text{LC}} = \pi r_c^2$, and $\Delta\Omega_{\text{LC}} = \pi(v_{D,R}/\bar{v}_\ell)^2$, we can use the results from chapter 2.2 to find

$$\mathcal{B}_T = \frac{\mathcal{F}_T^{\text{LC}}}{A_{\text{LC}}} \frac{1}{\Delta\Omega_{\text{LC}}} \frac{\bar{v}_\ell}{\Delta v_\ell} = \frac{2\mathcal{F}_S}{\pi A_{\text{LC}}} \left(\frac{v_c}{v_{D,R}} \right)^2 \sim \frac{2\mathcal{F}_S}{\pi A_{\text{LC}}} \frac{\gamma}{\omega_r} \quad (11)$$

The condition on the first factor is to keep exposure times reasonable, $\mathcal{F}_T^{\text{LC}}/A_{\text{LC}} \geq 10^{11}$ atom s $^{-1}$ mm $^{-2}$. For narrow feature width, say $\alpha \leq 1/50$, the beam spread is to be controlled, thus we choose collimation $\Delta\Omega \leq \pi(\alpha\lambda/2w_0)^2$ where we have assumed the thick lens focusing regime with $f \simeq w_0 \simeq 100\lambda$. For a thermal beam this leads to $1/\Delta\Omega_{\text{LC}} \geq 3 \times 10^7$. Brightness should hence exceed $\mathcal{B}_T \geq 3 \times 10^{18}$ atoms s $^{-1}$ mm $^{-2}$ srad, but not without fulfilling the conditions on flux density $\mathcal{F}_{\text{LC}}/A_{\text{LC}}$ and collimation $1/\Delta\Omega_{\text{LC}}$ (equation (10)) separately for meaningful ANF.

The most flexible parameter in the last part of equation (11) is the source flux \mathcal{F}_S . Since MOTs and atom lasers have much lower achievable flux than thermal beams, it is clear why thermal but transversely cooled sources are the best choice. In figure 7, we plot the total target surface area amenable to ANF in 1 min exposure vs the flux density available from several types of atomic beam sources.

For a rough estimate of the source flux required we take $A_{\text{LC}} = 1 \text{ mm}^2$, and since $1/\Delta\Omega_{\text{cap}} = (k\bar{v}_\ell/2\gamma)^2/\pi$ is typically of order $10^3\text{--}10^4$, we find that a thermal source producing $\mathcal{F}_S = \mathcal{F}_{\text{LC}}/\Delta\Omega_{\text{cap}} \geq 10^{14\text{--}15}$ atoms s $^{-1}$ is a good choice for ANF.

There are also upper limits to the intensity of an effusive thermal beam. An upper bound to the oven density ρ is found from the mean free path for atoms in the oven which should exceed the oven aperture d . We find $\rho < 1/\sigma d$, where σ is the hard-sphere collision cross section, typically 10^{-14} cm 2 . Thus, $\rho < 10^{15}$ atoms cm $^{-3}$, corresponding to a pressure below 3 Pa. For a 1 mm diameter oven aperture, the maximum flux

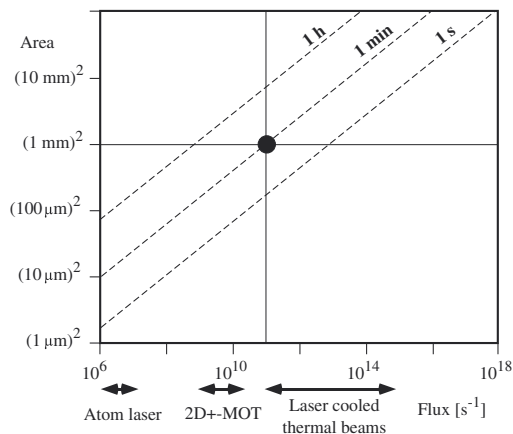


Figure 7. Physical properties of atomic beam sources. A deposition rate of 10^{11} atoms $s^{-1} mm^{-2}$ corresponds to 1 monolayer min^{-1} . The area is the target region covered by the atomic beam and the times are for one monolayer average exposure. Experiments have mostly been carried out near the black dot.

would then be $\mathcal{F} \sim \text{few} \times 10^{17}$ atoms s^{-1} , leaving 2–3 orders of magnitude as a dynamic source range for ANF.

Magneto-optical traps, etc. The MOT has become the workhorse of cold atom experiments. Low-velocity atoms with small absolute values of velocity spread are conveniently obtained from such a source, and several methods for the extraction of the trapped ensemble of atoms have been developed. One of the first of these was the low-velocity intense source [38] that produced a continuous beam of 5×10^9 atoms s^{-1} , and a variant of this described in [39]. Both of these produce about the same flux, with a longitudinal velocity spread $\Delta v_\ell < 1$ m s^{-1} , and divergences limited by transverse laser cooling or MOT temperatures. Equation (11) shows that B_T becomes smaller for lower T_S simply because the divergence angle increases for fixed transverse velocity spread.

Up to now there have been only two ANF experiments that extract atoms from such precooled sources [40, 41]. Reference [2] describes a 1 mm diameter Cs beam of nearly 3×10^{10} atoms s^{-1} at $\bar{v}_\ell \sim 100$ m s^{-1} with B limited only by the laser cooling process to 7×10^{17} atoms $s^{-1} mm^{-2} sr^{-1}$. Reference [42] describes a 1 mm diameter metastable Ne beam of 5×10^{10} atoms s^{-1} at $\bar{v}_\ell \sim 100$ m s^{-1} with B similarly limited to nearly 10^{16} atoms $s^{-1} mm^{-2} sr^{-1}$. Other beams have even higher brilliance or phase space density, but they all suffer from relatively low flux when considered for applications in ANF. This is because the total flux is the crucial experimental parameter since it determines the exposure time as discussed above, and angular spread or monochromaticity values below a certain threshold do little to improve ANF feature size. Thus atomic beam sources cooled in all three dimensions do not currently offer significant advantages for ANF.

Atom lasers. While conventional concepts of ‘ray optics’ have proven sufficient for most of these applications, more recently the extraction of atoms from Bose condensates has produced beams of coherent matter waves. Because of their close analogy to conventional lasers, they are called *atom lasers* and can approach the diffraction limit for atomic de Broglie

Table 3. Best feature values obtained for different atoms used in DD. For definitions see figure 4. Not all values may have been obtained under the same experimental conditions.

Atom	Subst.	Period (nm)	Width (nm)	Height (nm)	Contrast	Ref.
Na	Si	295	20	1.5	>0.9	[12, 61]
Cr	Si	213	29	47	>0.8	[13, 28]
Al	Si	155	70	2	>0.15	[53, 62]

waves. Their advent has crossed the borderline from classical atomic beams with particle like trajectories to coherent beams of matter waves [43–45].

Although such coherent beams of matter waves have extremely high phase space density Λ , their very low flux \mathcal{F} makes them unsuitable for ANF at present (see figure 7). For example, in [44] the phase space density Λ of the BEC is of the order unity and the quoted brightness, or radiance (not brilliance) is huge. But the source is pulsed, and there are only a few million atoms per pulse, and the repetition rate is surely less than 1 Hz, so the total flux is much too small for practical ANF. Still, the extremely high Λ of such sources promises superb atom optical properties whenever diffraction limited operation is essential. They may be useful for deposition into very small areas.

3.3. Elements for ANF

The basic requirement for DD is a suitable beam of atoms with a readily accessible laser transition. A suitable atomic beam can be made from an element whose vapour pressure can be raised to the order of 1 mbar with an oven temperature of ~ 1000 K or less. This includes the alkali metals and alkaline earths, as well as some transition elements and some group III atoms. A survey of currently known systems is given in table 3 in section 4.

Of course, any material that is a gas at room temperature is suitable, but the only atomic ones are the noble gases. The excitation energy of these is generally outside the range of readily available lasers, and so atomic beams are usually formed with metastable states of these atoms, typically 10–20 eV above the ground state. In fact, it is precisely this stored energy that makes these atoms suitable for NAL. The difficulty is that the metastable states are fragile, and typically can not be populated to a higher fraction than a few $\times 10^{-5}$ of the gas.

ANF is impractical with molecular gases for the same reason as laser cooling: molecules lack the required closed, cycling transitions because of their very many sublevels. Such closed transitions are required because laser cooling involves a large number of spontaneous emission events [1].

Figure 8 shows those elements that are, at least in principle, candidates for DD, i.e. that are susceptible for the application of light forces. For practical reasons we have omitted those elements whose resonance wavelengths are shorter than 300 nm. The figure includes all the favourite atoms of laser cooling, but also many elements of technological interest such as group III elements and transition metals.

While DD relies on just a single species, NAL requires an atom–surface combination which allows suitable chemical modifications. A survey of currently known systems is given

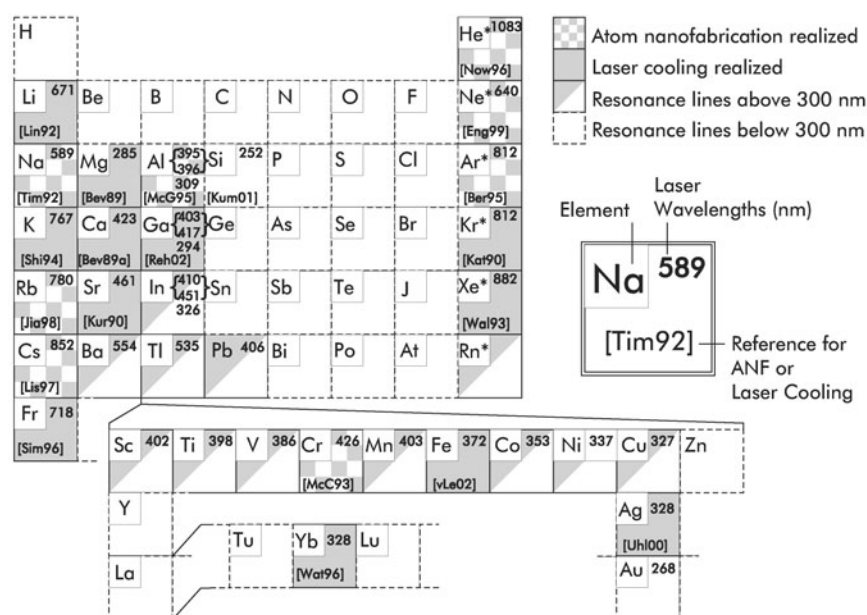


Figure 8. Atom nanofabrication in the periodic table of elements. Rare gas elements He, Ne, ... are used in their metastable triplet state. In the III. group up to 3 wavelengths may be required to achieve laser cooling [19, 46, 47, 40, 48–51, 30, 52, 22, 13, 53, 21, 54–56, 12, 57–59].

Table 4. Resist-surface-atom combinations for NAL.

Resist/Surface	Atom	Flux or flux density	Exp.-time	Resolution	Ref.
<i>Resists from SAM</i>					
AT (C ₁₂)/Au	Ar*	10 ¹⁴ at s ⁻¹ sr ⁻¹	1–4 h	<100 nm	[19]
AT (C ₁₂)/Au	He*	8 × 10 ¹¹ at s ⁻¹ cm ⁻²	6 min	30 nm	[21, 65, 67]
AT (C ₁₂)/Au	Ne*	1.5 × 10 ¹⁴ at s ⁻¹ sr ⁻¹	2–4 min		[40]
AT (C ₉)/Au	Cs	10 ¹⁴ at s ⁻¹ sr ⁻¹	1–10 min	<80 nm	[68, 69]
ODS/SiO–Si	Cs	1.3 × 10 ¹² at s ⁻¹ cm ⁻²	1–3 h	60 nm	[70]
ODS/SiO–Si	Ar*	2 × 10 ¹¹ at s ⁻¹ cm ⁻²	>15 h		[71]
OTS/SiO–Si	Ne*	1.5 × 10 ¹⁴ at s ⁻¹ sr ⁻¹	2–4 min		[40]
Si–H/Si	Ar*	2 × 10 ¹¹ at s ⁻¹ cm ⁻²	>3 h		[72]
<i>SAM protective layer formation</i>					
PPB/Rb–Cr	Rb	n.a.	3 min	n.a.	[48]
<i>Contamination resist formation</i>					
SiO ₂ –Si	Ar*	3 × 10 ¹¹ at s ⁻¹ cm ⁻²	21 h		[73]
GaAs	Ne*	4.6 × 10 ¹¹ at s ⁻¹ cm ⁻²	24 h	<50 nm	[74]
Si	Ne*	1.5 × 10 ¹⁴ at s ⁻¹ sr ⁻¹	4 h		[40]

Explanations: rare gas atoms are used in the metastable triplet state, indicated by '*'. SAM: self-assembled monolayer; AT (C_n): alkanethiole (CH₃(CH₂)_{n-1}SH) with chain length *n*; PPB: propylbenzoate; ODS: octadecylsiloxane; OTS: octadecyltrichlorosiloxane. More details (dosage, etching procedures) are given in the references. For the sake of comparability we have converted author's units into at s⁻¹ sr⁻¹ or at s⁻¹ cm⁻².

below in table 4 in section 4. The table shows a general tendency to combine an inert chemical surface with a highly reactive or activated atomic species.

4. Experimental results in ANF

4.1. Description of ANF structures

There are a few geometrical measures that characterize nanostructures of the type under discussion here, as shown in figure 4. The width, or FWHM, is a measure of the spatial resolution or smallest feature size. For DD, the height is determined by total beam flux and exposure time, whereas for NAL it depends on the resist and film preparation, as well as the etching process. For DD, the background can arise from many

sources, such as aberrations of the atom optical elements that pattern the atoms, other isotopes in the atomic beam, atoms in states that experience no optical force from the focusing light beams, etc. For NAL, the background also depends on the resist and the film, but can often be essentially zero. The period is related to the wavelength of the focusing light, but as discussed below, can be a small fraction of λ . The contrast, defined as the ratio of height to (height/height + pedestal) (see figure 4) is often a convenient figure of merit for DD.

4.2. Fabrication by DD

In DD the flux density pattern of an atomic beam modulated by the patterning mask is translated into the thickness variation of the layers of atoms deposited from the incident beam.

Thus, the nanostructure formation is achieved in a single step. Sometimes it is interesting to combine several methods of nanofabrication. As an example hybrid manufacture of arrays of magnetic wires was demonstrated [60].

Information about several experiments that have been used to make an array of parallel lines, along with some useful data, is collected in table 3.

4.2.1. First experiments with sodium. The first experimental results in the novel field of ANF were obtained in 1992 at the AT&T Bell Laboratories with directly deposited Na [12]. A thermal Na atomic beam was collimated by two-dimensional ‘Doppler’ optical molasses resulting in a divergence less than 0.6 mrad, patterned by a one-dimensional standing wave light field (300 μm diameter of the laser beam that constituted the light mask; laser intensity $I = 5 \text{ W cm}^{-2}$; detuning $\delta = -100 \text{ MHz} \sim -10\gamma$), and deposited onto a silicon substrate. Parallel lines separated by $\lambda/2 = 294 \text{ nm}$ were generated extending over 0.2 cm^2 . In this experiment, the linewidth and contrast of the highly reactive Na structures could not be determined because it oxidizes rapidly in air and there was no *in situ* diagnosis.

Later experiments with Na [61] were optimized by using the $\text{lin}\perp\text{lin}$ polarization gradient laser cooling scheme [1], reducing the divergence to less than 0.2 mrad. Furthermore the interaction length of the atoms with the standing wave was decreased by focusing the standing wave laser beam to a waist of $56 \mu\text{m}$, leading to a shorter atomic focal length. These improvements resulted in an unprecedented FWHM—linewidth of about 20 nm and a contrast > 0.9 , which was determined by an *in situ* scanning tunneling microscope (STM).

4.2.2. Robust ANF with chromium. Permanent and robust nanostructures that could be removed from the vacuum chamber were first produced by DD of Cr and described in 1993 [13]. The $\lambda = 425 \text{ nm}$ laser beams for the ${}^7\text{S}_3 \rightarrow {}^7\text{P}_4$ transition were derived from a single dye laser, and sidebands were generated by an acousto-optical modulator (AOM). A thermal Cr atomic beam was formed from an alumina crucible at a temperature of 1575°C , followed by a ‘sub-Doppler’ optical molasses in $\text{lin}\perp\text{lin}$ polarization gradient configuration that collimated the atomic beam divergence to less than 0.2 mrad.

For production of parallel lines spaced by $\lambda/2 = 213 \text{ nm}$, the light mask was formed by a one-dimensional standing wave with a waist of $400 \mu\text{m}$, power of 20 mW, and $200 \text{ MHz} \sim 40\gamma$ blue detuning. Parallel Cr lines extending over more than a mm^2 exhibiting a FWHM linewidth of 66 nm, a height of 34 nm, and a contrast of better than 0.5 was initially achieved (see figure 9). More detailed investigations [28] revealed that with the same setup and a systematic investigation the feature width could be narrowed to 29 nm and the contrast improved to a ratio of 0.8. Since calculations accounting for spherical and chromatic aberrations as well as beams spread were predicting a narrower feature width, the excess was attributed to the dynamics of Cr atoms once deposited on the surface. This assumption is supported by the observation of a feature width that decreases with total accumulated flux to a minimum and then increases again.

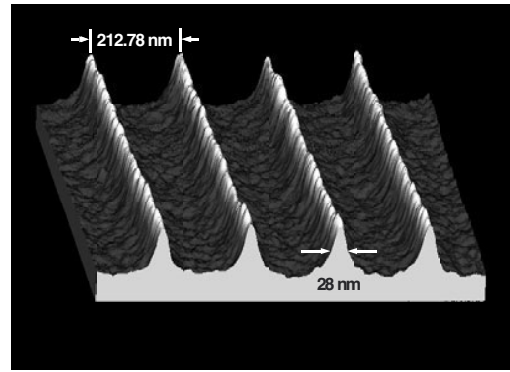


Figure 9. AFM-picture of directly deposited chromium lines. By permission of McClelland.

4.2.3. Lines separated by less than $\lambda/2$. For intensity gradients acting on an atomic beam the smallest spacing for an array of one-dimensional lines is $\lambda/2$. However, the internal magnetic structure of the atoms can also have important effects on optical forces as has been learned from sub-Doppler laser cooling [1]. Such polarization gradient forces have been exploited to produce arrays of lines with spatial periods of only $\lambda/8$ [63]. Using a two-dimensional light mask, structures of period $\lambda/3$ [16] (see below) have been manufactured. And more recently, blue diode lasers have been shown to deliver sufficiently intense light fields for DD with Cr atoms [64].

4.2.4. Aluminium nanostructures from uv-light masks. Elements of group III of the periodic table are of technological interest, and Al has also been used to make permanent nanostructures by DD [53]. UV-light was produced by frequency doubling the output of a 618 nm dye laser to drive the transition from the upper fine structure component of the Al ground state, $3^2\text{P}_{3/2}$, to the $3^2\text{D}_{5/2}$ excited state. It served both for optical collimation and for the light mask. The thermal atomic beam was generated at an oven temperature of 1400°C , and collimated in a two-dimensional optical molasses to a remaining divergence of 0.3 mrad. Parallel Lines with a periodicity of $\lambda/2 = 155 \text{ nm}$ FWHM, a linewidth of 70 nm, and a height of 3 on 20 nm background [62] could be produced. Since the upper fine structure state, $3^2\text{P}_{3/2}$, that was used for focusing in these experiments is thermally populated to only 25%, the contrast was limited to small values. This problem may be overcome by application of optical pumping through additional blue lasers.

4.3. Resist-based NAL

Resist-based NAL closely resembles the more traditional forms of lithography (figure 10). First a substrate is covered by a resist and placed into an exposure chamber (for NAL, this is an atomic beam vacuum chamber). A pattern is then applied by exposure to a beam of active atoms whose spatial distribution transmits the desired pattern to the resist. Then the substrate must be removed from the vacuum system and processed by standard lithographic techniques, typically wet chemistry (although there may be dry or ion etching techniques on the horizon, a combination has already been demonstrated by Lu *et al* [65]). Several atom–surface combinations have

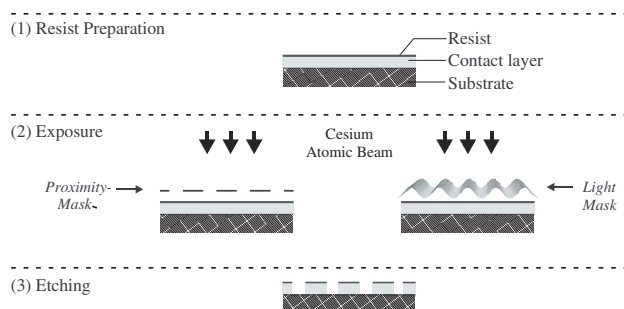


Figure 10. This illustrates the general principle of atom lithography. After the resist is prepared (1) the exposure may be done either through a proximity (2-left) or a light mask (2-right). Then the sample is removed from the vacuum system for etching (3).

been found to be effective for NAL, and information about them is collected in table 4.

NAL can be used to pattern almost any material that can be etched, and this includes refractory metals such as Fe and Ni whose magnetic properties may be of special utility. Its breadth makes it especially suitable for fabrication of useful specimens and devices. Among the other advantages of NAL are that it integrates readily into highly developed technologies for device production and nanostructure fabrication, and that the well-known baseline or background problem of DD is readily compensated.

4.3.1. SAMs, metastable rare gas atoms. NAL with metastable rare gases uses energy deposition to destroy bonds in the polymeric molecules of SAMs that constitute the resist [19, 36]. These organic monolayers are attractive since they can easily be formed by dipping the substrate into a suitable solution [66]. They are typically made up of long-chain molecules of alkanethiols that form oriented monolayers on a surface with their tails sticking upward, almost like the pile of an ordinary carpet. When significant energy is deposited onto one of these molecules, the chain is broken and the molecule is readily removed from the substrate in later processing. Metastable He (He^*) is a popular choice for this application because it has the capability of breaking the bonds in the longest of the SAM chains (typically 12 units) with high efficiency, and since these longer ones provide the most effective resistance against the subsequent etching, the frequency of accidental holes is greatly reduced. Since He^* carries more energy than any other metastable atom, it can do this with the lowest dosage, and consequently the fastest exposure and minimum restrictions on the atomic beams and laser control.

4.3.2. Alkalies. Alkali atoms are not only highly reactive but also excellent candidates for the application of laser cooling and light forces ([1]; see periodic table in figure 8). Hence experimenters set out to investigate whether alkalies could also be used to chemically modify surfaces such as SAMs. It was indeed demonstrated that results comparing well with metastable rare gases could be obtained with much shorter exposure times of order minutes or less [68, 69] (see table 4).

An example of simple structure generated with NAL is shown in figure 2 [22]. Here, light forces from a blue detuned standing wave were used to produce an array of parallel straight

lines etched into a 30 nm thick gold layer. Exposure times were typically several minutes, and the light mask was operated with conditions very closely resembling those used for writing parallel lines in DD experiments, i.e. ~ 10 mW of laser power and a few hundred megahertz red detuning from the atomic resonance frequency.

The resolution of this specific example is *a priori* limited to >30 nm by chemical processes resulting from the isotropic etching of the gold layer whose typical thickness is 30 nm. Another SAM, octylsiloxane (ODS), can be formed on Si surfaces covered by a native SiO_2 layer whose negligible thickness promises much improved resolution in etching processes. Spatial features <60 nm were generated to show the feasibility of this lithography process [70]. It was furthermore shown that rare gas atoms cause similar results with the ODS- SiO_2/Si surface [71] as well as with hydrogen-passivated silicon surfaces $\text{Si-H}/\text{Si}$ [72].

While most resists can be damaged for etching by the incident atomic beam, it is also possible to use alkalis as an agent to form a locally protective layer. An example of this approach has been achieved with a Rb/Cr surface exposed to a vapour of propylbenzoate [48].

4.3.3. Contamination resist formation. A protective layer can also be formed on a surface if, for instance, an adsorbed substance is chemically modified. Although there is no detailed understanding at the molecular level, there is good experimental evidence that the formation of a durable carbonaceous resist occurs in the presence of dilute hydrocarbon vapours (vacuum pump oil) [40, 73, 74]. Good resolution down to about 50 nm has been achieved, but this ‘contamination resist’ method suffers from long exposure times of order hours. Furthermore, the hydrocarbons are undesirable in many manufacturing processes.

4.3.4. Internal state coding of a pattern. By optical quenching of the metastable state, it is possible to show that its large internal energy, of order 10 eV for Ar, is responsible for the chemical modification of the SAM. Since metastable atoms are generated through electron collisions in the beam (efficiency $\leq 10^{-5}$) they have generally low flux resulting in hour long exposure times to obtain a dose of 6–10 Ar atoms per SAM molecule necessary for good etching contrast. Similar contrast results were obtained with a much smaller dose of 0.3 metastable He^* atoms per molecule [21]. Thus, the high efficiency of the He^* atom, which may be attributed to its large internal energy of about 20 eV, translates into a much shorter exposure time than for other atoms.

Chemical atom-surface interactions are dramatically different for metastable atoms than for their quenched counterpart. With a beam of metastable atoms it is not only possible to provide a pattern through flux density modulation of an atomic beam, as is the case for NAL, but also with a spatial modulation of the internal atomic state populations. For instance, a standing wave of light may cause some atoms to de-excite everywhere except near the nodes of the standing wave field. Because saturation of the quenching transition is highly nonlinear, this process can select reactive atoms in very narrow channels near the optical nodes. The feature size in such an experiment [23, 75] is then only limited by quantum

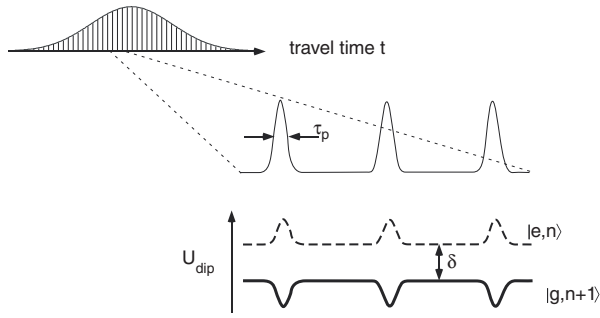


Figure 11. Time evolution of the effective dipole potential acting on an atom exposed to a modelocked laser. Upper left: an atom traverses a light field and interacts successively with many individual light pulses. Centre from top to bottom: pulses with length τ_p cause level shifts reflecting the pulse shape and intensity in the dressed states $|e, n\rangle$ (---, unpopulated) and $|g, n+1\rangle$ (—, always populated). Here e, g indicate the atomic excited and ground state, and n the number of photons in the driving field. At exact resonance these levels are degenerate. For $\tau_p \delta \gg 1$ an atom in the ground state adiabatically follows the effective potential suggested by the lowest trace and experiences a force derived from the corresponding average potential.

mechanical diffraction of the atomic de Broglie wave, rather than by atom optical aberrations of the atom optical lens array.

4.4. Focusing with pulsed lasers

An efficient optical dipole force is not necessarily related to continuous atom laser interaction. For instance, although an atom subject to a train of pulses drawn from a typical modelocked laser (pulse width $\tau_p = 100$ fs–100 ps, pulse separation 12.5 ns) is nearly always in the dark, it may experience very strong forces during the presence of the pulse. An average dipole potential can be attributed to atom laser interaction provided the adiabatic condition $\tau_p \delta \gg 1$ is fulfilled, where δ is the detuning characterizing the dipole force in equation (2). In figure 11 a short intuitive explanation in terms of the so-called ‘dressed atom model’ is shown [1]. It was experimentally demonstrated that a standing wave derived from a train of intense laser pulses with 80 ps length and 80 MHz repetition rate is able to focus Cs atoms and carry out NAL in exact analogy with a cw laser [76].

5. Complex structures

More complex structures than simple one-dimensional arrays of straight lines have already been constructed. A two-dimensional light mask was composed for chromium; McClelland *et al* [14] generated a quadratic mask configuration by crossing two one-dimensional standing waves across the substrate at 90° . The resulting pattern consisted of quadratically arranged chromium features on an area of 0.02 mm². These features had a height of 12 nm, their FWHM-width was 80 ± 10 nm, respectively.

Drodofsky *et al* [15] produced Cr-structures arranged in a hexagonal lattice through interference of three laser beams crossing the substrate at 120° ; at positive detuning the deposited chromium forms a honeycomb structure, at negative detuning Cr-dots arrange in a hexagonal symmetry (see figure 12). Also intensity variations of the contributing

laser beams generate diverse features arranged in hexagonal symmetry. Furthermore, a superlattice has been deposited by a small angular misalignment of laser beams in a quadratic symmetry [17].

Standing waves containing polarization gradients can generate structures with separation even less than $\lambda/2$. At NIST, parallel Cr-lines separated by $\lambda/8$ have been deposited [63], using a one-dimensional standing wave in $\text{lin} \perp \text{lin}$ configuration. In Konstanz a two-dimensional hexagonal light mask in a variant of the $\text{lin} \perp \text{lin}$ configuration generated a two-dimensional pattern of chromium with $\lambda/3$ feature spacing [16]. This is attributed to avoided crossings arising from Raman coherences induced between magnetic sublevels of the chromium atom.

5.1. Patterning properties of light masks

The optical dipole force causes the flux density of atomic beams to be modulated by the gradients of the induced light shift when it traverses the light mask. The pattern of the intensity distribution is thereby transferred to a surface, either by one step DD or by NAL involving several steps of processing. The modulated light field thus acts as an immaterial *light mask* and determines the layout of the fabricated structure with lens like properties as discussed in section 2.2.

Disregarding the influence of polarization, any intensity distribution $I(x, y)$ is generated from a superposition of electromagnetic waves E_i :

$$\left| \sum_i E_{0i} e^{-i(\omega t + \phi_i)} e^{i(k_{xi}x + k_{yi}y)} \right|^2 \rightarrow I(x, y). \quad (12)$$

As a rule of thumb, each laser beam with a new direction of the \mathbf{k}_i -vector adds a new degree of freedom to the pattern formed by the light field. With relatively few laser beams the pattern and its symmetries remain transparent and are easily recognized. Synthesis of the light field is obtained with beamsplitters and mirrors, as was demonstrated in several experiments [15–17, 63] and summarized in figure 12.

How complex the structures to be generated with light masks may be and what types of structures can be generated remains an open question. In equation (12) it is straightforward to predict the intensity pattern from the electromagnetic waves known and properly arranged in an experiment. The so-called *inverse problem*, however, is very difficult to treat. The solution to the mathematical problem

$$I(x, y) \rightarrow \left| \sum_i E_{0i} e^{-i(\omega t + \phi_i)} e^{i(k_{xi}x + k_{yi}y)} \right|^2 \quad (13)$$

is not known in general, and if it is known, it usually requires a multitude of laser beams to be superposed with interferometric precision.

5.1.1. Multiple beam generation. A complex pattern generated from multiple beams by superposition from beamsplitters and mirrors becomes rapidly very clumsy. This problem, however, can be solved through the application of well-known optical components capable of transforming simple laser beams into more complicated wavefronts

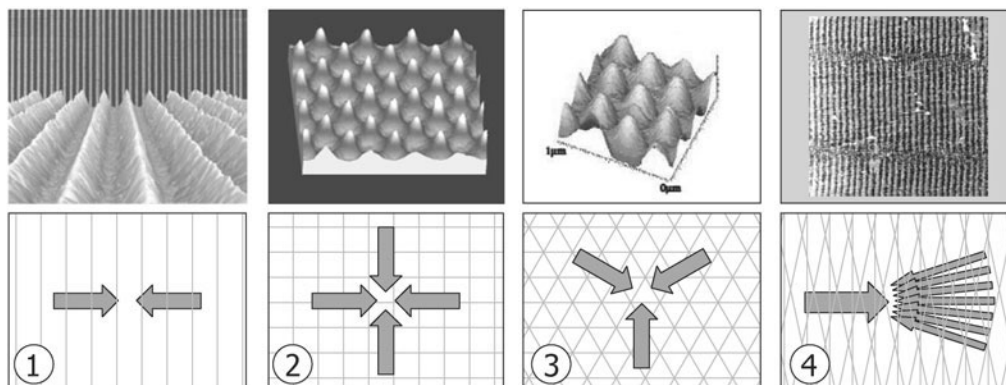


Figure 12. Gallery of structures generated through ANF. From left to right: one-dimensional standing wave makes straight Cr-lines [13]; rectangular light mask from crossed standing waves generates rectangular pattern of Cr dots [14]; 3 laser beams at 120° make hexagonal Cr pattern [15]; multi beam light mask generated from a volume hologram makes complex pattern [18]. With permission by McClelland and Pfau.

including diffractive optical elements, volume holograms, controllable mirrors or liquid crystal phase arrays. A volume hologram was prepared and demonstrated to be applicable for the generation of a complex pattern [18, 77]. Analysis of the pattern was simplified in this case since the pattern was generated by interference of the diffracted waves with the strong incoming read-out wave (see below). The experiment also demonstrated that fractional, ‘weak’ intensity modulation of the light mask is acceptable.

5.1.2. The inverse problem. A known and desired pattern $I(x, y)$ mathematically requires the solution of the so-called *inverse problem* suggested by equation (13). This requires the establishment of a configuration of electromagnetic waves $\Re\{E_i e^{-i(\omega t - \mathbf{k}_i \cdot \mathbf{r})}\}$ that reproduces, or least approximates, the pattern by interference [78]. Since the pattern is constructed through interference of individual beams with wave vectors \mathbf{k}_i , it is natural to investigate the pattern formed in \mathbf{k} - or reciprocal space. The pattern is in general composed from all possible difference vectors $\mathbf{k}_i - \mathbf{k}_j = \mathbf{\kappa}_{ij}$.

If one beam is much stronger than all others, only the difference vectors with this beam will contribute efficiently to pattern formation. Mathematically, in this weak modulation case, we have

$$I(x, y) = \frac{c\epsilon_0}{2} \left| E_0 e^{-i\omega t} e^{i(kx)} + \sum_i \epsilon_i e^{-i(\omega t + \phi_i)} e^{i(k_{xi}x + k_{yi}y)} \right|^2$$

$$\approx I_0 \left(1 + \Re e \left\{ \sum_i \frac{\epsilon_i^*}{E_0} e^{i((k-k_{xi})x - k_{yi}y)} \right\} + \mathcal{O} \left(\frac{\epsilon_i \epsilon_j}{|E_0|^2} \right) \right) \quad (14)$$

which much resembles a conventional Fourier expansion. The \mathbf{k} -space of such a situation, corresponding to the right most example figure 12, is shown in figure 13. However, wavevectors are still restricted to the two full circles in figure 13, and conventional Fourier transform can still not be applied.

The \mathbf{k} -space picture helps to rapidly understand the pattern of figure 12(4). The primitive vectors of the Brillouin zone form a two-dimensional-rhombohedral structure, while the four-fold symmetry apparent in figure 12 is also easily identified in reciprocal space.

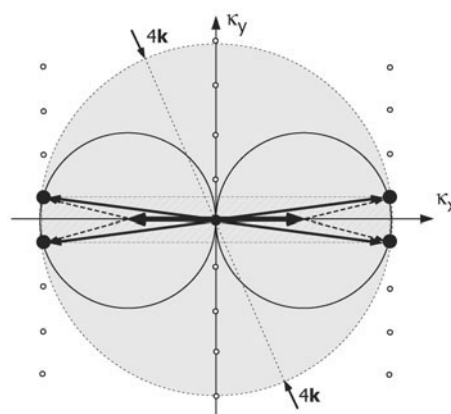


Figure 13. A simple example of reciprocal space for light mask generation corresponding to the example from [18, 77] and figure 12. The hatched area shows the primitive Brillouin zone which is two-dimensional-rhombohedral in this case. The central thick pair of arrow indicates the original and strong read-out beam, dashed arrows mark the weaker diffracted beams. The geometry of the pattern is determined from the difference vectors. For a single read-out beam all possible $\vec{\kappa}$ -vector differences are located on the two circles with radius $r = |\mathbf{k}|$. In general, any difference vector within $\kappa \leq 2|\mathbf{k}|$ can be realized.

5.2. ANF for materials with modulated composition—three-dimensional nanofabrication

In ANF, light masks act on selected elements only because of their resonance conditions. If a crystal is grown from several constituents simultaneously, e.g. a III–V semiconductor mixed crystal such as (In, Al)As, DD has the potential to generate spatial modulation of their composition. Modulation periods are at visible wavelengths and hence the corresponding structure may influence optical, electronic, and magnetic properties of the solid.

One very interesting perspective is the growth of novel materials with truly three-dimensional structure, i.e. a superlattice, at nanometre scales. It is obvious that optical dipole forces will cause lateral modulation of the growth process while the composition in the third dimension is controlled by regulating the flux of the constituents.

While it is probably straightforward to implement geometric arrangements for this novel method, dynamics of the growth process will decide whether useful new materials will ultimately be produced with this novel method. Let us point out here that for materials with modulated composition generated with this method a narrow feature width (see section 2.2.2) is less important than good contrast.

A first step in this direction was taken in Konstanz [79] where an array of straight lines of Cr was deposited along with a layer of MgF_2 as host material. The Cr atomic beam was patterned by a one-dimensional standing wave, generating a periodically modulated Cr density within the host material at macroscopic concentrations. Auger electron analysis revealed that the relative concentration of the constituents remains constant.

5.3. Some applications of light mask ANF

5.3.1. Rulers. Although complex pattern generation is possible (see section 5) a very natural application of ANF using light masks is the precise generation of large scale periodic structures from simple standing waves useful for length metrology at small scales in microscopy. Several experiments have been carried out [80, 81] and have demonstrated that a resolution of at least 1 in 10^6 can be achieved.

5.3.2. Magnetic nanowire arrays. The corrugated Cr surface produced through DD (see figure 9) was used by Tulchinsky *et al* [60] to manufacture an array of magnetic nanowires. The sample was irradiated at grazing incidence (10°) such that the Cr peaks acted as an array of shadow masks and iron was deposited on the slopes oriented towards the beam source. The process resulted in the fabrication of ferromagnetic lines with 100 nm width and 20–40 nm height exhibiting magnetic domains with a typical length of 10 μm .

5.4. ANF with atomic pencils

Nanostructure generation atom by atom has become a celebrated method [82–84] with local scanning probe tools such as the atomic force microscope. With cantilevers, individual atoms or molecules are manipulated on a surface one at a time providing ultimate atomic resolution. The process is serial and slow at an individual site, however, and hence conceptual interest in this method remains open.

Recently it was shown that a cantilever perforated with a very small aperture ranging from 50 to 250 nm can be used as a shadow mask to directly deposit a structure of, e.g. copper wire [85]. With a source of 2 mm diameter and mounted 60 mm away deposition rates of $0.1\text{--}2\text{ nm min}^{-1}$ were obtained. Interestingly enough, the aperture was not clogged by the atomic beam but remained open. It was shown that controlled excursions of the movable sample underneath the cantilever would result in a correspondingly complex structure. Parallel application of this method with many holes ('nanosieves') is also conceivable [86].

Light forces may potentially be used to enhance performance of the atomic pencil: with laser cooling, atoms emitted from the source can be collimated first (see section 3.1) and then concentrated [87] onto the aperture in order to

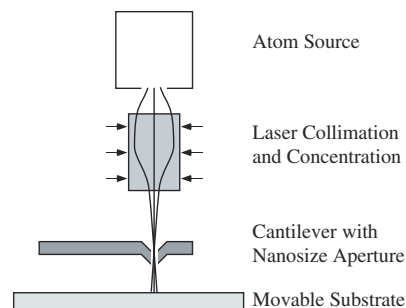


Figure 14. Concept of an atomic pencil for versatile writing of complex nanostructures.

accelerate writing speed (figure 14). Atomic pencils could then serve as versatile nanowiring tools. The low kinetic energy of atoms deposited by the atom pencil method may for instance result in better conduction properties than in nanowires fabricated with energetic focused ion beams.

Optical dipole forces have also been suggested to be used [88, 89], e.g. as a near field lens inside an aperture of sub wavelength size, promising focusing to a spot of only a few nanometre. In all cases, the atomic flux will usually limit the applicability.

6. ANF and matter waves

Matter waves have recently been celebrated as the beginning of a new era where conventional atomic beams may be replaced by atom lasers, much in the spirit that for many applications classical light sources have been replaced by coherent laser beams over the past 40–50 years [44, 45, 90, 91]. Consequently ANF is also frequently quoted as an important field of application for coherent matter waves. No experiments have been reported to date, however, in section 3.2, we have already been led to the conclusion that the role of atom lasers in ANF with currently available and foreseeable technology will probably be limited to the exposure of very small samples and areas since, their total flux is very small. Breakthroughs in the performance of atom lasers could rapidly change this situation, of course.

Several concepts for the influence and application of the wave nature of atoms in ANF have been developed, and in some cases even been tested. These lines of research are briefly presented in the following.

6.1. Beyond ray optics

In analogy to conventional optics, the wave nature of matter becomes apparent in diffraction and other interference effects. Theoretically, the Kirchhoff treatment of diffraction of visible light leading to Fraunhofer and Fresnel limits is perfectly appropriate to describe diffraction of atomic matter waves. A necessary condition for the observation of diffraction is transverse coherence, quantitatively measured through the 'visibility' of interference fringes. While this condition is intrinsically met with atom lasers, it can also always be fulfilled with classical sources of radiation by reducing the aperture of the source. Although this causes a strong reduction in flux which impairs the usefulness of classical atomic sources

for ANF as outlined in section 3.2, a number of inspiring demonstration experiments has been carried out indicating the possible role of matter waves. Note that, in contrast to conventional waves, the atomic constituents of a coherent matter wave undergo s-wave collisions hence causing an intrinsic nonlinearity that has already been demonstrated in the field of nonlinear atom optics. This interaction adds a new element to wave propagation [92] which is well-known from the Gross–Pitaevski equation.

It is natural that most concepts draw on analogies with well-known concepts in light optics. For instance in [93] near field interferences such as the Talbot imaging were suggested to improve resolution in ANF. A theoretical suggestion was also made to transform plane matter waves into a de Broglie wavefront of arbitrary shape through a series of spatially controlled measurements [94].

6.2. Atom holography

Holography has been perceived as an ultimate optical art of imaging ever since its invention [95, 96], owing to its unique capability of reconstructing full complete wavefronts leaving an object which is thus observed with its three-dimensional appearance. In optics, holographic recording or fabrication of the actual hologram is usually carried out by recording the interference of the light scattered from the object (the signal wave) with a reference wave. Diffracting the reference wave from the hologram then reconstructs the original signal wave. Holographic recording with atoms has not been attempted to date. It has long been known [97], however, that holograms can also be constructed theoretically, e.g. by a computer and then read-out as before. In the laboratory of Shimizu [41, 98] such holograms have been designed and produced by electron beam lithography. The holograms were illuminated from a source of laser-cooled metastable Ne^* atoms with a very small effective aperture in order to achieve sufficient transverse coherence. The extremely high detection efficiency of the metastable Ne atoms by means of a multichannel plate allowed this experiment to be carried out with no more than a total of 10^5 accumulated atoms.

The authors encoded different letters into their holograms. Two examples of their beautiful results can be seen in figure 15: in the first image the letter ‘F’ was reconstructed from a pure plane amplitude hologram (holes of order $0.1 \mu\text{m}$ diameter in a SiN membrane). Several diffraction orders of the hologram can be seen.

In a more recent series of experiments, several manipulations of the holograms were implemented in order to improve image quality, resulting in the second image. For these modifications the curvature of the wavefront of the incoming atoms was accounted for by substituting Fresnel for Fraunhofer approximation [99]. Furthermore, electrodes were integrated into the experiment enabling phase control of atoms through the Stark effect. These modifications allowed the experimenters to sharpen the images, to suppress unwanted orders of diffraction and even to electrically switch between different holograms [100–102].

The width of the reconstructed letters is of order 1 mm, and the resolution is $60 \mu\text{m}$ because of the diffraction geometry of the experiment. Ultimately, the resolution is limited by

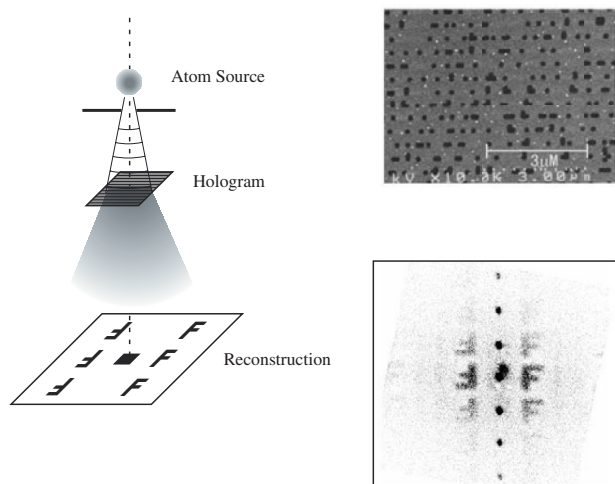


Figure 15. Schematic drawing for image reconstruction by atom holography. In experiments a classical source with very small aperture was used to enable transverse coherence, but may be replaced by an atom laser in the future. The hologram is designed by computer and realized with a SiN membrane with square holes. The picture shows an SEM image, courtesy and permission of Shimizu [99].

the de Broglie wavelength of the atoms to several nm only, making atom holography indeed an interesting candidate for ANF with matter waves. Technically, it is not yet possible to realize this limit since it involves further reduction of the aperture and hence atomic flux. For example, the holograms shown in figure 15 took many hours to record. Even so the impressive list of achievements proves the applicability of even the most sophisticated interferometric concepts to matter waves. Very recently it was shown that reflection-type devices can be constructed with excellent quality to perform holographic imaging with atomic matter waves [103].

7. Magnetic imaging for ANF

Optical or charged particle imaging systems providing demagnification of material masks constitute one of the most important processing steps in nanostructure fabrication. In analogy with these methods, we discuss the potential of magnetic atom optical elements for structure formation at the nanometre scale. It is in principle known how to construct reflective and refractive optical elements. The applicability of these elements for ANF hinges on the technical quality that can be achieved. The optical dipole force used for ANF can also be used to construct imaging components such as lenses and mirrors. However, magnetic components often complement the capabilities for applications since they are passive components and do not require operation of laser light sources.

Magnetic forces acting on atomic beams are derived from inhomogeneous magnetic fields, that initiated atom optics. In the famous Stern Gerlach experiment in 1921 [3, 4] an atomic beam was deflected by the magnetic force from an inhomogeneous magnetic field. Later on, magnetic hexapole fields were used [7, 104] to focus paramagnetic atomic and molecular beams. The scale of the force is limited by the Bohr magneton $\mu_B = e\hbar/mc$, and for thermal atomic beams, the

refractive power of available magnetic lenses is small, causing long focal lengths, typically of order 1 m and more. The advent of laser-cooled atomic beams has drastically changed this situation, since they bring the focal length to the cm range and allow the reduction of aberrations caused by longitudinal velocity spread. The general feasibility of magnetic imaging with a magnetic hexapole lens and a slow atomic beam has been shown at mm scales by Kaenders *et al* [105]. A recent survey of motional control for laser-cooled atoms with magnetic forces was given by Hinds and Hughes [106].

7.1. Atom optical elements with magnetic forces

Atoms with unpaired electrons are generally paramagnetic, including metastable rare gas atoms, and thus subject to forces in an inhomogeneous magnetic field. An atom with magnetic moment μ in a magnetic field \mathbf{B} has an interaction energy

$$U_{\text{mag}}(\mathbf{r}) = -\mu \cdot \mathbf{B}(\mathbf{r}) \quad (15)$$

and the force is given by its gradient $\mathbf{F}(\mathbf{r}) = \nabla(\mu \cdot \mathbf{B}(\mathbf{r}))$. Since we are interested here in the motional properties of paramagnetic atoms, we will mostly neglect details of the relative orientation of atom and field, and assume that the atoms are always prepared in a state which is antiparallel and fully aligned with the field in the stretched m -state. These are the low-field seekers that have $\mu \cdot \mathbf{B}(\mathbf{r}) = -\mu B(\mathbf{r})$. Evaluation of the force is simplified in this important special case, and we find $\mathbf{F}(\mathbf{r}) = -\nabla(\mu B(\mathbf{r}))$. Furthermore we can take the magnetic moment in the extreme states to be independent of the magnetic field and hence write

$$\mathbf{F}(\mathbf{r}) = -g\mu_B \nabla B(\mathbf{r}), \quad (16)$$

where g is the atomic Landé factor. Magnetic atom optical elements are therefore determined by the distribution of the modulus of the magnetic field which translates into an effective potential $U_{\text{mag}} = g\mu_B |B(\mathbf{r})|$.

7.1.1. Magnetic lenses. Magnetic hexapole fields were used as early as 1951 [7, 104] as lenses to focus beams of paramagnetic atoms and molecules. Large chromatic aberration and long focal lengths caused by the velocity distribution of a thermal atomic beam in these early experiments can be overcome when laser cooling is employed to prepare slow atomic beams with narrow velocity spread [105]. Refractive components [10] such as magnetic lenses or axicons are derived from cylindrical arrangements of currents or magnetized material with azimuthal periodicity. Figure 16 shows simple components made from homogeneously magnetized permanent magnetic material.

Construction of pure magnetic multipoles from permanent magnets was pioneered by Halbach [107, 108]. It became known that continuous cylindrical rotation of homogeneous magnetization M_0 ($\mathbf{M}(\rho, \phi) = M_0(\cos(n\phi)\mathbf{e}_\rho + \sin(n\phi)\mathbf{e}_\phi)$) results in a perfect plane magnetic multipole of order n inside the bore with radius $\rho = \rho_0$ of such a system. The corresponding potential, $\Phi_M = B_n/n(\rho/\rho_0)^n \cos(n\phi)$ where $B_n \sim \mu_0 M_0$ depends on details of the geometry [107], gives rise to a field $\mathbf{B} = B_n(\rho/\rho_0)^{n-1}(\cos(n\phi)\mathbf{e}_\rho - \sin(n\phi)\mathbf{e}_\phi)$. The motion of properly oriented atoms is then determined only by the modulus of the magnetic field amplitude,

$$B(\rho, \phi) = B_n \left(\frac{\rho}{\rho_0} \right)^{n-1}. \quad (17)$$

For $n = 2$ a quadrupolar field grows linearly with ρ corresponding to an optical axicon, for the $n = 3$ hexapole field we find harmonic variation making a magnetic lens for paramagnetic atoms (figure 16).

In reality, continuous rotation is approximated through a system of segments with stepwise rotated magnetization. Strong permanent magnets have allowed the construction of magnetic lenses with focal lengths as short as a few centimetre for atomic beams travelling at 10–100 m s⁻¹. Such a lens was

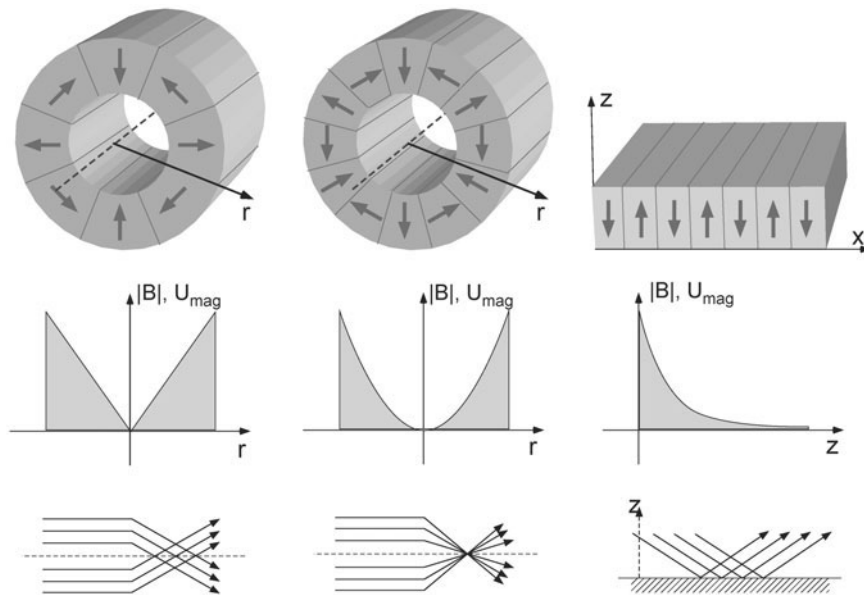


Figure 16. Construction of magnetic multipoles from hard permanent magnetic materials with periodic magnetization. From left to right: upper row: cylindrical quadrupole (magnetic ‘axicon’) and hexapole (magnetic lens), plane periodic array (magnetic mirror); middle: leading terms of the effective magnetic potential; lower row: typical particle beam trajectories.

used to demonstrate image formation with an atomic beam [105] at the mm scale. The quest for very small structures is impaired by image distortion dominated by chromatic aberrations which can be estimated by $\Delta\rho \sim D \cdot \Delta v/v$ for the radius $\Delta\rho$ of least confusion and an input beam diameter D . Hence a 1 mm beam would need $\Delta v/v \leq 10^{-3}$ to enter the sub-micrometer domain, which is possible but costly to prepare. New prospects may arise when coherent matter waves become more widely available as was recently shown by Bloch *et al* [109] (see section 6).

7.1.2. Magnetic mirrors. It has been known for a very long time that reflective optics is superior to refractive optics if dominated by chromatic aberrations, and smooth magnetic potential surfaces can be used to construct magnetic mirrors for paramagnetic atoms. Atom optical mirrors can also be obtained with the evanescent light-wave of total internal reflection [110]. For robust applications, however, we expect magnetic mirrors to have an edge over evanescent light-wave mirrors: they are passive components, do not require laser light and can easily subtend a large area.

A plane permanent magnetic mirror (PMM) surface can be obtained ‘unwinding’ the previous cylindrical concept of Halbach. Alternatively, sinusoidal modulation of a corresponding plane current density distribution with period Λ along the plane can be used to create a current carrying mirror (CCM) [111, 112]:

$$\begin{aligned} \text{PMM: } \mathbf{M}(\mathbf{r}) &= M_0 \left(\cos\left(\frac{2\pi x}{\Lambda}\right) \mathbf{e}_x + \sin\left(\frac{2\pi x}{\Lambda}\right) \mathbf{e}_z \right) \\ \text{CCM: } \mathbf{I}(\mathbf{r}) &= I_0 \sin\left(\frac{2\pi x}{\Lambda}\right) \mathbf{e}_y. \end{aligned} \quad (18)$$

In the neighbourhood of the surface a magnetic field is generated with rapidly rotating direction $\mathbf{B}(\mathbf{r}) = B(z)((\sin(2\pi x/\Lambda)\mathbf{e}_x + \cos(2\pi x/\Lambda)\mathbf{e}_y)$ but with a modulus that only depends on the separation from the surface [106, 112]. Its scaling length is controlled by the period length $\Lambda = 2\pi/k$ of the magnetization or current distribution, and for a mirror extending to infinity we find

$$|\mathbf{B}(x, y)| = B_0 e^{-ky} \quad \text{with } B_0 = \begin{cases} \alpha_M \cdot \mu_0 M_0 & \text{PMM} \\ \alpha_I \cdot \frac{\mu_0 I}{\Lambda} & \text{CCM} \end{cases} \quad (19)$$

The surface field strengths B_0 depends on magnetization and current density, respectively, and a geometrical factor $\alpha_{M,I} \leq 1$. It varies with separation from the surface only.

The perfect mirror is formed by an infinitely high potential (large surface field strength for large reflectivity) with infinite steepness (short Λ for negligible chromatic aberrations), and perfect flatness (low imaging distortions). Table 5 summarizes properties of magnetic mirrors achieved in recent experiments.

In reality, continuous variation of magnetization and current density is approximated by a segmented array of magnetic material and wires. This segmentation causes a corrugation of the magnetic field amplitude and hence instead of equation (19) the magnetic amplitude follows

$$|\mathbf{B}(x, y)| = \alpha_{M,I} B_0 e^{-ky} [1 + \beta_{M,I} \cos(2kx)e^{-ky} + \dots], \quad (20)$$

where $\beta_{M,I}$ is another geometric factor of order 1 or smaller. Since the corrugation rapidly reduces with distance y from the surface, improved mirror flatness can be expected at larger distances, at the expense of an effectively reduced surface field strength.

7.2. Permanent magnetic mirrors

Large surface field strength is conveniently available from state of the art hard permanent magnetic materials ($\mu_r \simeq 1$) such as SmCo or NdFeB with magnetization $M_0/\mu_0 > 1$ T, provided the slabs in figure 17 have $b \gg \Lambda$ in order to obtain a geometric factor $a_M = (1 - e^{-2\pi b/\Lambda}) \approx 1$. Excellent reflectivity can then be obtained for atoms travelling with kinetic energy $KE/k_B = \mu_B B_0/k_B \leq 1$ K towards the surface which is easily achieved with laser-cooled atoms.

Magnetic mirrors with strong surface field strengths have been constructed from permanent magnetic materials [113, 114]. Conventional manufacturing methods segment by segment do not allow simple routes for obtaining short periods Λ , however, so that scaling lengths of order mm have been used. The smoothness of such devices is conceptually impaired by several effects: segmentation and finite size causing corrugation may be ‘controlled’ by staying away from the surface and adding compensation components such as special segments made from hard [113] or soft [25] magnetic material. Imperfections such as geometric tolerances, magnetization fluctuations, etc cause, however, long range distortions of the mirror surface yielding deformed images [25]. It has also been shown that ‘natural’ magnetic surfaces such as a cobalt single crystal [116] do show good reflectivity suggesting that control of the domain pattern could make a good mirror.

Table 5. A survey of magnetic mirrors for atom optics.

Type of mirror	B_0 (T)	Period Λ	Angular spread	Ref.
<i>Permanent magnet arrays, flat</i>				
NdFeB slabs	0.5	2 mm	Poor flatness	[113, 114]
Sintered NdFeB	1.2	1–10 μm		[115]
Co single crystal	1.2	30 μm	54 mrad	[116]
CoCr	0.03	1–4 μm	16 mrad	[117]
<i>Micro-electromagnet mirrors, flat</i>				
Ag, Au, Cu, Nb wires	0.1	12–200 μm	13 mrad	[118]
<i>Magnetic recording material, flat</i>				
Audio tape	0.01	13–30 μm		[119]
Video tape	0.05	30 μm	6 mrad	[120]
TbFeCo films	0.08	1.2 μm		[121]
<i>Curved mirrors</i>				
Video tape	0.01	13–30 μm		[120, 122]

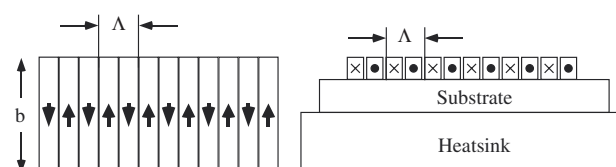


Figure 17. Geometry of magnetic mirror for paramagnetic atoms made from permanent magnets (PMM, left) and current loops (CCM, right).

Much better quality atom optical results have been obtained in the laboratory of Hinds [106] with mirrors constructed from magnetic recording material such as video tapes or floppy discs. Although strong magnetization material is used for such components, the geometry factor is generally small, $\alpha_M \ll 1$, and hence cold atoms are essential for their application. Within this restriction it has been shown that good quality atom optical properties (multiple reflections, focusing, etc, measured through the angular spread at specular reflection, table 5) with short periodicities of order $10 \mu\text{m}$ are readily obtained with these materials. Limitations seem to be imposed by inhomogeneities in the media [120] and magnetization [121]. The shortest periods to date have been obtained by Sidorov *et al* [117] who manufactured grooved magnetic structures replicated from a nickel master with periods extending below $1 \mu\text{m}$ and demonstrated good atom optical quality.

Multiple reflections with large reflectivity have been demonstrated with video tape mirrors used at grazing incidence for atoms travelling at moderate velocities [122]. This result shows that more sophisticated mirror arrangements, for instance the Wolter telescope [123] used for imaging at grazing incidence with x-rays, could potentially be implemented with atomic beams, too.

7.3. Current carrying mirrors

The creation of magnetic mirrors from arrays of wires is attractive since microelectronic manufacturing methods are available with superb precision. Short period length ($\Lambda \geq 1 \mu\text{m}$) and acceptable mirror flatness is readily achieved. In several experiments the applicability of CCMs has been realized with good results [118, 124] for cold atoms.

The surface field strengths derived from an array of alternating current carrying wires is $B_0 = \mu_0 I / \Lambda$. We can calculate that a linear current density of $I \geq 1 \text{ A } \mu\text{m}^{-1}$ is required to match the 1 T field strength derived from permanent magnets at the mirror surface. A $10 \mu\text{m}$ wide copper wire thus needs a 10 A current. With a cross section of $10 \times 1 \mu^2$ a 1 cm^2 area covered with this wire makes a $17 \text{ k}\Omega$ resistance requiring multi kW power dissipation to be removed from this small area. Hence CCMs seem to be limited to periodicities of about $50 \mu\text{m}$.

7.4. Status of magnetic projection imaging

Magnetic mirrors offer a conceptually convincing route towards image formation with an atomic beam, and the general feasibility of these atom optical devices has been demonstrated, mostly with cold atoms. While there is no fundamental obstacle, to date atom optical magnetic mirror have not fulfilled requirements to be successful with very high resolution in the sub-micrometre domain. Although CMMs currently offer the best choice in terms of a steep potential and precision manufacturing, they are essentially useful only for very slow atoms which in turn (see section 3.1) are of limited use for ANF. Successful and precise generation of PMMs at lengths scales below $10 \mu\text{m}$ is advancing [121] and could, however, offer a promising route towards magnetic image formation for ANF.

8. Conclusions and outlook

The race for miniaturization with ever smaller structures is a scientific and engineering endeavour which we will briefly contrast here with the potentials of ANF. While the original driving force for miniaturization is scientific, the still accelerating pace of this ongoing development is overwhelmingly set by economic mechanisms having led to the current status of the microelectronic industry [125]. This evolution is most clearly stated by Moore's law which predicts the doubling of the number of transistors on a semiconductor chip every 18 months. The semiconductor industry has transformed this prediction into a roadmap [126] towards ever smaller structures.

To date and beyond expectations optical lithography alone has made this technological achievement possible (see table 6). Multiply corrected imaging systems as well as advanced mask technologies such as phase shift masking [130] have led to a situation where for a given wavelength the Rayleigh diffraction limit of resolution can always be met. For instance today, in 2002, KrF excimer lasers with $\lambda = 248 \text{ nm}$ allow widespread structure generation down to the 130 nm level, and with the introduction of ArF ($\lambda = 193 \text{ nm}$) and F_2 ($\lambda = 157 \text{ nm}$) laser sources decreased pitch values of 90 nm and 65 nm can be foreseen for 2004 and 2007, respectively (table 6). At this level of resolution the gate region of a CMOS transistor continues to operate much like its larger scale relatives, and hence the quest for even smaller structures amenable for mass production is expected to continue. It is currently assumed that extension of manufacturing methods beyond the 65 nm limit must be accompanied by a qualitative change in lithography methods since neither suitable light sources nor optical imaging systems are currently available at these wavelengths. The quest for next generation lithography (NGL) methods hence remains open, although EUV methods employing light sources at $\lambda = 13 \text{ nm}$ appear to be the currently favoured candidate. This situation certainly stimulates research for novel methods.

Charged particle lithography relies on resist-based processing steps and is conceptually very similar to optical lithography. At 10 keV electron and ion beams offer short wavelengths in the sub-nanometre domain, and resolution is not bound by the diffraction limit but by other deficiencies at the order of a few nanometre. An alternative method for fabrication of nanoscale structures at the industrial level [127], however, must not only produce small and narrow feature sizes, but also meet further requirements, e.g. tight tolerances (so-called critical dimension (CD) control), throughput, and many more. The lack of a suitable mask comparable to optical lithography and overcoming serial pattern production has prevented e-beams and ion-beams from fulfilling these extended requirements, even though they have been used and intensely developed for decades. They are, however, indispensable tools for optical mask manufacture and other purposes.

Scanning probe tools have been widely studied means of nanofabrication. They provide ultimate, i.e. atomic resolution demonstrated in beautiful experiments [82] and have inspired many suggestions for applications. Still, the universal applicability of this method is by no means substantiated, and hence the application of scanning probe nanofabrication

Table 6. Overview: methods of nanofabrication. Recent developments are routinely documented in the Nov/Dec issue of the *J. Vac. Sci. Technol. B*, collecting new results from the annual ‘Electron, Ion and Photon Beam Technology and Nanofabrication’ Conference.

Method	λ	Resolution	Strengths, limitations	Ref.
<i>Optical methods</i>				
UV-light	248 nm	130 nm	Industry standard 2002; 65 nm resolution with $\lambda = 157$ nm planned 2007	[126]
EUV-light	13 nm	35 nm	Frontrunner for NGL	[126]
<i>Charged particle beam methods</i>				
Electron beams Ion beams	<1 nm	5 nm	Very high resolution; lack of mask technology	[127, 128]
<i>Atomic methods</i>				
SPN	n.a.	Atomic	Ultimate, i.e. atomic resolution	[129]
ANF	<1 nm	30 nm	Periodic structures; direct writing, three-dimensional structured crystal growth	This paper

(SPN) remains an important topic for research laboratories. ANF outlined in this paper has in common with SPN that it directly tries to influence the deposition position of matter at the atomic level on a surface, at least in the DD branch of ANF. Important differences are that ANF without effort manipulates up to 10^{17} atoms s^{-1} while SPN essentially controls one atom or molecule at a time with a single cantilever. ANF on the other hand will most likely never realize the atomic level of resolution intrinsic to SPN.

In conclusion it would be presumptuous to consider ANF to be a serious candidate for replacing optical lithography or any other nanofabrication method for mass production. From the current perspective, ANF may have a competitive edge in scientific and potentially industrial applications where periodic structures play an important role, where the crystal growth of crystals is manipulated in all three dimensions, or where direct writing of structures with certain elements at nanometre scales is of interest.

Acknowledgments

Over the past years many physicists have contributed with their hands and minds to advance atom nanofabrication in our laboratories: D Haubrich, H J Adams, R Bertram, I Bloch, M Kreis, F Lison, M Mützel, H Merimeche, P Schuh, S Tandler and others. Some experiments have been carried out in fruitful collaboration with the research groups of J Mlynek, Konstanz and E A Hinds, Sussex. Our work would have been impossible without continuing support by the state of Northrhine-Westfalia, the Deutsche Forschungsgemeinschaft, the BMBF, and the European Commission (in particular the now ending TMR network *Nanofab*). Further funds for collaboration have been supplied by the Academic Research Council (UK), the Procope programme of the DAAD, the Alexander von Humboldt foundation, the Office of Naval Research and the National Science Foundation (both USA).

References

- [1] Metcalf H and van der Straten P 1999 *Laser Cooling and Trapping* (New York: Springer)
- [2] Lison F, Schuh P, Haubrich D and Meschede D 2000 High brilliance Zeeman-slowed cesium atomic beam *Phys. Rev. A* **61** 1–9
- [3] Stern O 1921 Der Weg zur experimentellen Prüfung der Richtungsquantelung im Magnetfeld *Z. Phys.* **7** 249–53
- [4] Gerlach W and Stern O 1921 Der experimentelle Nachweis des magnetischen Moments des Silberatoms *Z. Phys.* **8** 110–11
- [5] Frisch O 1933 Experimenteller Nachweis des Einsteinschen Strahlungsrückstoßes *Z. Physik* **86** 42
- [6] Adams C S, Sigel M and Mlynek J 1994 Atom optics *Phys. Rep.* **240** 143
- [7] Friedburg H and Paul W 1951 Optische Abbildung mit neutralen Atomen *Naturwissenschaften* **38** 159–60
- [8] Christensen R and Hamilton D 1959 Permanent magnet for atomic beam focusing *Rev. Sci. Instrum.* **30** 356
- [9] Metcalf H 1984 Magnetic trapping of decelerated neutral atoms *Prog. Quant. Electr.* **8** 169–75
- [10] Kaenders W G, Lison F, Muller I, Richter A, Wynands R and Meschede D 1996 Refractive components for magnetic atom optics *Phys. Rev. A* **54** 5067–75
- [11] Folman R, Krüger P, Cassetari D, Hessmo B, Maier T and Schmiedmayer J 2000 Controlling cold atoms using nanofabricated surfaces: atom chips *Phys. Rev. Lett.* **84** 4749–52
- [12] Timp G, Behringer R E, Tennant D M, Cunningham J E, Prentiss M and Berggren K K 1992 Using light as a lens for submicron, neutral-atom lithography *Phys. Rev. Lett.* **69** 1636
- [13] McClelland J J, Scholten R E, Palm E C and Celotta R 1993 Laser-focused atomic deposition *Science* **262** 87
- [14] Gupta R, McClelland J J, Jabbour Z J and Celotta R 1995 Nanofabrication of a two-dimensional array using laser-focussed atomic deposition *Appl. Phys. Lett.* **67** 1378
- [15] Drodofsky U, Stuhler J, Schulze T, Drewsen M, Brezger B, Pfau T and Mlynek J 1997 Hexagonal nanostructures generated by light masks for neutral atoms *Appl. Phys. B* **65** 755
- [16] Brezger B, Schulze T, Schmidt P O, Mertens R, Pfau T and Mlynek J 1999 Polarization gradient light masks in atom lithography *Europhys. Lett.* **46** 148–53
- [17] Schulze T, Brezger B, Mertens R, Pivk M, Pfau T and Mlynek J 2000 Writing a superlattice with light forces *Appl. Phys. B* **70** 671–4
- [18] Mützel M, Tandler S, Haubrich D, Meschede D, Peithmann K, Flaspöhler M and Buse K 2002 Atom lithography with a holographic light mask *Phys. Rev. Lett.* **83** 083601–1–4
- [19] Berggren K K, Bard A, Wilbur J L, Gillaspay J D, Helg A G, McClelland J J, Rolston S L, Phillips W D, Prentiss M and Whitesides G M 1995 Microlithography by using neutral metastable atoms and self-assembled monolayers *Science* **269** 1255
- [20] Senefelder A 1771–1834 Alois Senefelder (born in Prague, worked in Munich, died in Munich) invented Lithography in the 18th century. Lithography relies on the modification of wetting properties of stones used for printing.
- [21] Nowak S, Pfau T and Mlynek J 1996 Nanolithography with metastable helium *Appl. Phys. B* **63** 203

- [22] Lison F, Haubrich D, Schuh P and Meschede D 1997 Nanostructure generation with a cesium atomic beam and an immaterial light mask *Appl. Phys. B* **65** 419
- [23] Johnson K S, Thywissen J H, Dekker N H, Berggren K K, Chu A P, Younkun R and Prentiss M 1998 Localization of metastable atom beams with optical standing waves: nanolithography at the Heisenberg limit *Science* **280** 1583–6
- [24] van der Stam K M R, te Sligte E, Smeets B, Bosch R C M, van der Straten P, Scholten R E, Beijerinck H C W and van Leeuwen K A H Modelling of nanostructure broadening in direct-write atom lithography *Phys. Rev. B* submitted
- [25] Lison F 1998 Atomlithographie und reflexive Atomoptik mit laserpräparierten Atomen *PhD Thesis* (University of Bonn)
- [26] McClelland J J 1995 Atom-optical properties of a standing-wave light-field *J. Opt. Soc. Am. B* **12** 1761–8
- [27] McClelland J J and Scheinfein M R 1991 Laser focusing of atoms: a particle-optics approach *J. Opt. Soc. Am. B* **8** 1974
- [28] Anderson W R, Bradley C C, McClelland J J and Celotta R J 1999 Minimizing feature width in atom optically fabricated chromium nanostructures *Phys. Rev. A* **59** 2476
- [29] Berggren K K, Prentiss M, Timp G and Behringer R E 1994 Calculation of atomic positions in nanometer-scale direct-write optical lithography with an optical standing wave *J. Opt. Soc. Am. B* **11** 1166–76
- [30] van Leeuwen K A H 2002 Private communication
- [31] Lee C J 2000 Quantum-mechanical analysis of atom lithography *Phys. Rev. A* **61** 063604–1–9
- [32] Villain J, Pimpinelli A, Tang L and Wolf D 1992 Terrace sizes in molecular beam epitaxy *J. Phys. I* **2** 2107–21
- [33] Pimpinelli A, Villain J and Wolf D E 1993 Fractal terraces in MBE growth *J. Phys. I* **3** 447–57
- [34] Jurdik E, Rasing Th, van Kempen H, Bradley C C and McClelland J J 1999 Surface growth in laser-focused atomic deposition *Phys. Rev. B* **60** 1543
- [35] Bradley R M, Eschmann A and Lee S A 2000 Theory of feature broadening in direct-write optical lithography *J. Appl. Phys.* **88** 3316
- [36] Close J D, Baldwin K G H, Hoffmann K and Quaas N 2000 Fragmentation of dodecanethiol molecules: application to self-assembled monolayer damage in atom lithography *Appl. Phys. B* **70** 651–6
- [37] Dalibard J and Cohen-Tannoudji C 1989 Laser cooling below the Doppler limit by polarization gradients—simple theoretical models *J. Opt. Soc. Am. B* **6** 2023–45
- [38] Lu Z T, Corwin K I, Renn M J, Anderson M H, Cornell E A and Wieman C E 1996 Low-velocity intense source of atoms from a magneto-optical trap *Phys. Rev. Lett.* **77** 3331
- [39] Kim K H, Lee K I, Noh H R, Jhe W, Kwon N and Ohtsu M 2001 Cold atomic beam produced by a conical mirror funnel *Phys. Rev. A* **64** 013402
- [40] Engels P, Salewski S, Levsen H, Sengstock K and Ertmer W 1999 Atom lithography with a cold, metastable neon beam *Appl. Phys. B* **69** 407–12
- [41] Fujita J, Morinaga M, Kishimoto T, Yasuda M, Matsui S and Shimizu F 1996 Manipulation of an atomic beam by a computer-generated hologram *Nature* **380** 691–4
- [42] Tempelaars J G C, Stas R J W, Sebel P G M, Beijerinck H C W and Vredendregt E J D 2002 An intense, slow and cold beam of metastable Ne(3s) 3P_2 atoms *Europhys. J. D* **18** 113–21
- [43] Andrews M R, Townsend C G, Miesner J J, Durfee D S, Stamper-Kurn D M and Ketterle W 1997 Observation of interference between two Bose condensates *Science* **275** 637
- [44] Bloch I, Hänsch T W and Esslinger T 1999 Atom laser with a cw output coupler *Phys. Rev. Lett.* **82** 3008
- [45] Hagley E, Deng L, Kozuma M, Wen J, Helmerson K, Rolston S L and Phillips W D 1999 A well-collimated quasi-continuous atom laser *Science* **283** 1706
- [46] Beverini N, De Pascalis S, Maccioni E, Pereira D, Strumia F, Vissani G, Wang Y Z and Novero C 1989 Evidence for laser cooling in a magnesium atomic beam *Opt. Lett.* **14** 350–2
- [47] Beverini N, Giammanco F, Maccioni E, Strumia F and Vissani G 1989 Measurement of the calcium $^1P_1-^1D_2$ transition rate in a laser-cooled atomic beam *J. Opt. Soc. Am. B* **6** 2188–93
- [48] Jiang H-B, Grossmann A and Hänsch T W 1998 Self-assembled monolayer of propylbenzoate on the bimetallic surface of Rb/Cr *Appl. Phys. A* **66** 119–22
- [49] Katori H and Shimizu F 1990 Laser cooling and trapping of argon and krypton using diode lasers *Japan. J. Appl. Phys.* **29** L2124–6
- [50] Kumagai H, Asakawa Y, Fujii T, Midorikawa K and Obara M 2001 High-power deep-uv cw coherent light source for laser cooling of silicon atoms *RIKEN Rev.* **33** 3
- [51] Kurosu T and Shimizu F 1990 Laser cooling and trapping of calcium and strontium *Japan. J. Appl. Phys.* **29** L2127–9
- [52] Lin Z, Shimizu K, Zhan M, Shimizu F and Takuma H 1992 Laser cooling and trapping of Li *Japan. J. Appl. Phys.* **30**
- [53] McGowan R W, Giltner D M and Lee S A 1995 Light force cooling, focusing and nanometer-scale deposition of aluminum atoms *Opt. Lett.* **20** 2535
- [54] Rehse S J and Lee S A 2002 *Laser Collimation of a Ga Atomic Beam* to be published
- [55] Shifang L and Clauser J F 1994 Diode-laser production of collimated slow cold potassium beams and crossover resonances *Phys. Rev. A* **49** 2702–13
- [56] Simsarian J E, Ghosh A, Orozco L A, Sprouse G D and Voytas P A 1996 Magneto-optical trapping of ^{210}Fr *Phys. Rev. Lett.* **76** 3522
- [57] Uhlenberg G, Dirscherl J and Walther H 2000 Magneto-optical trapping of silver atoms *Phys. Rev. A* **62** 3404
- [58] Walhout M, Megens H J L, Witte A and Rolston S L 1993 Magneto-optical trapping of metastable xenon: isotope-shift measurements *Phys. Rev. A* **48** R879
- [59] Watanabe M, Ohmukai R, Tanaka U, Hayasaka K, Imajo H and Urabe S 1996 Velocity control of an Yb beam by a frequency-doubled mode-locked laser *J. Opt. Soc. Am. B* **13** 2377
- [60] Tulchinsky D A, Kelley M H, McClelland J J, Gupta R and Celotta R J 1998 Fabrication and domain imaging of iron magnetic nanowire arrays *J. Vac. Sci. Technol.* **16** 1817
- [61] Natarajan V, Behringer R and Timp G 1996 High-contrast, high-resolution focusing of neutral atoms using light forces *Phys. Rev. A* **53** 4381–5
- [62] Rehse S J, McGowan R W and Lee S A 2000 Optical manipulation of group III atoms *Appl. Phys. B* **70** 657–60
- [63] Gupta R, McClelland J J, Marte P and Celotta R 1996 Raman-induced avoided crossings in adiabatic optical potentials: observation of $\lambda/8$ spatial frequency in the distribution of atoms *Phys. Rev. Lett.* **76** 4689–92
- [64] Sun H B, Inouye H, Inouye Y, Okamoto K and Kawata S 2001 Laser-diode-tuned sequential laser atom cooling and trapping for nanofabrications *Japan. J. Appl. Phys.* **40** L711–14
- [65] Lu W, Baldwin K G H, Hoogerland M D, Buckman S J, Senden T J, Sheridan T E and Boswell R W 1998 Sharp edged silicon structures generated using atom lithography with metastable helium atoms *J. Vac. Sci. Technol. B* **16** 3846–9
- [66] Bell A S, Pfau T, Drodofsky U, Stuhler J, Schulze T, Brezger B, Nowak S and Mlynek J 1998 Atomic lithography *Microelectron. Eng.* **41–42** 587
- [67] Bard A, Berggren K K, Wilbur J L, Gillaspay J D, Rolston S L, McClelland J J, Phillips W D, Prentiss M and Whitesides G M 1997 Self-assembled monolayers exposed by metastable argon and metastable helium for neutral atom lithography and atomic beam imaging *J. Vac. Sci. Technol. B* **15** 1805

- [68] Kreis M, Lison F, Haubrich D, Schuh P, Meschede D, Nowak S, Pfau T and Mlynek J 1996 Pattern generation with cesium atomic beams at nanometer scales *Appl. Phys. B* **63** 649
- [69] Berggren K K, Younkin R, Cheung E, Prentiss M, Black A, Whitesides G M, Ralph D C, Black C T and Tinkham M 1997 Demonstration of a nanolithographic technique using a self-assembled monolayer resist for neutral atomic cesium *Adv. Mater.* **9** 52
- [70] Younkin R, Berggren K K, Johnson K S, Prentiss M, Ralph D C and Whitesides G M 1997 Nanostructure fabrication in silicon using cesium to pattern a self-assembled monolayer *Appl. Phys. Lett.* **71** 1261
- [71] Hill S B, Haich C A, Dunning F B, Walters G K, McClelland J J, Celotta R, Craighead H G, Han J and Tanenbaum D M 1999 Patterning of octadecylsiloxane self-assembled monolayers on Si(100) using Ar($^3P_{0,2}$) atoms *J. Vac. Sci. Technol. B* **17** 1087
- [72] Hill S B, Haich C A, Dunning F B, Walters G K, McClelland J J, Celotta R and Craighead H G 1999 Patterning of hydrogen-passivated Si(100) using Ar($^3P_{0,2}$) metastable atoms *Appl. Phys. Lett.* **74** 2239
- [73] Johnson K S *et al* 1996 Using neutral metastable argon atoms and contamination lithography to form nanostructures in silicon, silicon dioxide and gold *Appl. Phys. Lett.* **69** 2773
- [74] Rehse S J, Glueck A D, Lee S A, Goulakov A B, Menoni C S, Ralph D C, Johnson K S and Prentiss M 1997 Nanolithography with metastable neon atoms: enhanced rate of contamination resist formation for nanostructure fabrication *Appl. Phys. Lett.* **71** 1427–9
- [75] Chu A P, Johnson K S and Prentiss M 1997 A virtual amplitude grating for atomic optics *Opt. Commun.* **134** 105–11
- [76] Mützel M, Haubrich D and Meschede D 2000 Nanoscale focusing of atoms with a pulsed standing wave *Appl. Phys. B* **70** 689–94
- [77] Mützel M, Burstedde C, Meschede D, Peithmann K and Buse K 2002 Atomic nanofabrication with complex light fields *Appl. Phys. B* in preparation
- [78] Burstedde C 2002 Approximate solution of a subproblem in interferometric atom lithography *Comp. Phys.* submitted
- [79] Schulze T, Mütter T, Jürgens D, Brezger B, Oberthaler M, Pfau T and Mlynek J 2001 Structured doping with light forces *Appl. Phys. Lett.* **78** 1781
- [80] Thywissen J H, Johnson K S, Dekker N H, Prentiss M, Wong S S, Weiss K and Grunze M 1998 Metastable-atom-activated growth of an ultrathin carbonaceous resist for reactive ion etching of SiO₂ and Si₃N₄ *J. Vac. Sci. Technol. B* **16** 1155
- [81] Jurdik E, Hohlfeld J, van Kempen H, Rasing Th and McClelland J J 2002 Laser-focused nanofabrication: Beating of two atomic resonances *Appl. Phys. Lett.* **80** 4443–5
- [82] Eigler D M and Schweizer E K 1990 Positioning single atoms with a scanning tunnelling microscope *Nature* **344** 524
- [83] Quate C F 1997 Scanning probes as a lithography tool for nanostructures *Surf. Sci.* **386** 259
- [84] Gimzewski J K and Joachim C 1999 Nanoscale science of single molecules using local probes *Science* **283** 1683
- [85] Lüthi R, Schlittler R R, Brugger J, Vettiger P, Welland M E and Gimzewski J K 1999 Parallel nanodevice fabrication using a combination of shadow mask and scanning probe methods *Appl. Phys. Lett.* **75** 1314–16
- [86] Brugger J, Berenschot J W, Kuiper S, Nijdam W, Otter B and Elwenspoek M 2000 Resistless patterning of sub-micron structures by evaporation through nanostencils *Microelectr. Eng.* **53** 403–5
- [87] Nellessen J, Werner J and Ertmer W 1990 Magneto-optical compression of a monoenergetic sodium atomic beam *Opt. Commun.* **78** 300–8
- [88] Balykin V I, Klimov V V and Letokhov V S 1994 Laser near field lens for atoms *J. Phys. II France* **4** 1981–97
- [89] Dubetsky B and Berman P R 1998 Conical lens for atom focusing *Phys. Rev. A* **58** 2413–16
- [90] Mewes M-O, Andrews M R, Kurn D M, Durfee D S, Townsend C G and Ketterle W 1997 Output coupler for Bose–Einstein condensed atoms *Phys. Rev. Lett.* **78** 582–5
- [91] Anderson B P and Kasevich M 1998 Macroscopic quantum interference from atomic tunnel arrays *Science* **282** 1686
- [92] Meystre P 2001 Nonlinear optics of de Broglie waves *Advances in Atomic, Molecular and Optical Physics* vol 47, ed B Bederson and H Walther (New York: Academic) pp 1–52
- [93] Meneghini S, Savichev V I, Leeuwen K A H and Schleich W P 2000 Atomic focusing and near field imaging for producing small-period nanostructures *Appl. Phys. B* **70** 675–82
- [94] Olshani M, Dekker N, Herzog C and Prentiss M 2000 de Broglie wave-front engineering *Phys. Rev. A* **62** 033612–1–4
- [95] Gabor D 1948 A new microscopic principle *Nature* **161** 777–8
- [96] Leith E N and Upatnieks J 1962 Reconstructed wavefronts and communication theory *J. Opt. Soc. Am.* **52** 1123–30
- [97] Brown B R and Lohmann A W 1966 Complex spatial filtering with binary masks *Appl. Opt.* **5** 967–9
- [98] Morinaga M, Yasuda M, Kishimoto T, Shimizu F, Fujita J and Matsui S 1996 Holographic manipulation of a cold atomic beam *Phys. Rev. Lett.* **77** 802–5
- [99] Fujita J, Kishimoto T, Morinaga M, Matsui S and Shimizu F 1998 Atomic beam holography for nanofabrication *J. Vac. Sci. Technol.* **16** 3855–8
- [100] Fujita J, Kishimoto T, Mitake S and Shimizu F 1999 Electric-field modified atomic beam holography *J. Vac. Sci. Technol.* **17** 2953–6
- [101] Fujita J, Mitake S and Shimizu F 2000 Interferometric modulation of an atomic beam by an electric field: a phase hologram for atoms *Phys. Rev. Lett.* **84** 4027–30
- [102] Fujita J, Mitake S and Shimizu F 2000 Real time pattern changing in atomic beam holography using phase shift by Stark shift *J. Vac. Sci. Technol.* **18** 3590–3
- [103] Shimizu F and Fujita J 2002 Reflection-type hologram for atoms *Phys. Rev. Lett.* **88** 123201
- [104] Friedburg H 1951 Optische Abbildung mit neutralen Atomen *Z. Physik.* **130** 493–512
- [105] Kaenders W, Lison F, Richter A, Wynands R and Meschede D 1995 Imaging with an atomic beam *Nature* **375** 214
- [106] Hinds E A and Hughes I G 1999 Magnetic atom optics: mirrors, guides, traps and chips for atoms *J. Phys. D: Appl. Phys.* **32** R119–46
- [107] Halbach K 1980 Design of permanent multipole magnets with rare earth cobalt material *Nucl. Instrum. Methods* **169** 1
- [108] Halbach K 1981 Physical and optical properties of rare earth cobalt magnets *Nucl. Instrum. Methods* **187** 109
- [109] Bloch I, Kohl M, Greiner M, Hänsch T W and Esslinger T 2001 Optics with an atom laser beam—*Phys. Rev. Lett.* **87** 030401
- [110] Dowling J and Gea-Banacloche J 1996 Evanescent light-wave atom mirrors, resonators, waveguides and traps *Adv. At. Mol. Opt. Phys.* **37** 1–94
- [111] Vladimirkii V V 1960 Magnetic mirrors, channels and bottles for cold neutrons *Zh. Eksp. Teor. Fiz.* **39** 1062
Vladimirkii V V 1960 *Sov. Phys. JETP* **12** 740
- [112] Opat G I, Wark S J and Cimmino A 1992 Electric and magnetic mirrors and gratings for slowly moving neutral atoms and molecules *Appl. Phys. B* **54** 396–402
- [113] Sidorov A, McLean R J, Rowlands W J, Lau D C, Murphy J E, Walciewicz M, Opat G I and Hannaford P 1996 Specular reflection of cold caesium atoms from a magnetostatic mirror *Quant. Semiclass. Opt.* **8** 713–25
- [114] Meschede D, Bloch I, Goepfert A, Haubrich D, Kreis M, Lison F, Schütze R and Wynands R 1997 Atom optics with permanent magnetic components *Atom Optics* vol 2995, ed M G Prentiss and W Phillips, pp 191–7 (*Proc. SPIE*)

- [115] Lison F, Haubrich D, Schuh P and Meschede D 1999 Reflection of a slow cesium atomic beam from a naturally magnetized Nd-Fe-B surface *Appl. Phys. B* **69** 501-4
- [116] Rosenbusch P, Retter J A, Hinds E A, Lison F, Haubrich D and Meschede D 2000 Reflection of cold atoms by a cobalt single crystal *Appl. Phys. B* **70** 661-3
- [117] Sidorov A I, McLean R J, Scharberg F, Gough D S, Davis T J, Sexton B J, Opat G I and Hannaford P 2002 Permanent-magnet microstructures for atom optics *Acta Phys. Pol.* **33** 2137
- [118] Drndic M, Zabow G, Lee C S, Thywissen J H, Johnson K S, Prentiss M, Westervelt R M, Featonby P P, Savalli V, Cognet L, Helmersen K, Westbrook N, Westbrook C I, Phillips W D and Aspect A 1999 Properties of microelectromagnet mirrors as reflectors of cold Rb atoms *Phys. Rev. A* **60** 4012-15
- [119] Roach T M, Abele H, Boshier M G, Grossman H L, Zetie K P and Hinds E A 1995 Realization of a magnetic mirror for cold atoms *Phys. Rev. Lett.* **75** 629
- [120] Saba C, Barton P A, Boshier M G, Hughes I G, Rosenbusch P, Sauer B E and Hinds E A 1999 Reconstruction of a cold atom cloud by magnetic focusing *Phys. Rev. Lett.* **82** 468
- [121] Sidorov A I, McLean R J, Gough D S, Davis T J, Akulshin A, Opat G I and Hannaford P 2001 Micron-scale magnetic structures for atom optics *Compt. Rendus Ser. IV* **2** 565-72
- [122] Bertram R, Merimeche H, Metcalf H, Haubrich D, Meschede D, Rosenbusch P and Hinds E A 2001 A whispering gallery mirror for atoms *Phys. Rev. A* **053405-1**
- [123] Wolter H 1952 Spiegelsysteme streifenden Einfalls als abbildende Optiken für Röntgenstrahlen *Ann. Phys.* **6** 94
- [124] Lau D C, Sidorov A I, Opat G I, McLean R J, Rowlands W J and Hannaford P 1999 Reflection of cold atoms from an array of current-carrying wires *Eur. Phys. J. D* **5** 193-9
- [125] Hutcheson G D and Hutcheson J D 1996 Technology and economics in the semiconductor industry *Sci. Am.* 40-6
- [126] 2002 International technology roadmap for semiconductors <http://public.itrs.net/Homepage>
- [127] Pease R F, Han L, Winograd G I, Meisburger W D, Packard D and McCord M A 2000 Prospects for charged particle lithography as a manufacturing tool *Microelectron. Eng.* **53** 55-60
- [128] Loeschner H *et al* 2002 Large-field particle beam optics for projection and proximity printing and for mask-less lithography (ml2) *JMMM*
- [129] Wilder K, Quate C F, Singh B and Kyser D F 1998 Electron beam and scanning probe lithography: a comparison *J. Vac. Sci. Technol. B* **16** 3864-73
- [130] Levenson M D 1993 Wavefront engineering for photolithography *Phys. Today* 28-36